Combustion and Flame 261 (2024) 113313

Contents lists available at ScienceDirect

Combustion and Flame

journal homepage: www.sciencedirect.com/journal/combustion-and-flame

Diffusive-thermal instabilities in unstrained H_2O-diluted syngas diffusion flames

Elie Antar *, Etienne Robert

Department of Mechanical Engineering, Polytechnique Montréal, Montréal, Québec H3T 1J4, Canada

ARTICLE INFO

Keywords:
Unstrained
Diffusion flame
Diffusive-thermal instabilities
Syngas
H_2O dilution

ABSTRACT

A new version of the unstrained diffusion flame burner that can be operated with gaseous fuels containing high vapor content is introduced. Being a good approximation of the classical chambered diffusion flame solution, the flames generated are nominally unstrained, unlike common research burners where hydrodynamic effects are significant. This permits quantitative comparison with theoretical models that are often based on this simple configuration, and paves the way for fundamental experimental studies with vaporized fuels. In this paper, the capabilities of the new burner design are exploited to study diffusive-thermal instabilities (DTIs) in H_2O-diluted H_2-CO-CH_4-CO_2 mixtures. H_2O dilution can be significant in biomass-derived syngas mixtures that are not cooled prior to combustion, and that are often burned directly to lower losses as waste heat and pollutant emission in practical combustors. Flammability limits are first presented for a broad range of fuel blends, where the destabilizing effect of H_2O dilution is discussed. Instability maps in terms of the Damköhler number are then provided to illustrate the different types of superimposed cellular-pulsating instabilities that onset from the simultaneous presence of H_2 with high diffusivity, and CO/CH_4 with much lower mobility. The characteristics of these peculiar instabilities are highly dependent on the H_2O dilution fraction, which increases both the fuel blend and oxidizer Lewis numbers. The degree of cellularity superimposed in the pulsating multi-fuel flame is reduced at higher water content, as the number of observed cells decreases. The opposite effect is observed on the pulsation frequency, which increases at higher water concentrations.

1. Introduction

The urgency to reduce greenhouse gas emissions has contributed to a surge in alternative energy carriers research over the past decades, particularly hydrogen-rich fuels such as syngas. Composed mainly of H_2 and CO, syngas can be produced via different thermochemical processes such as gasification or pyrolysis, and from a multitude of renewable and potentially carbon-neutral biomass feedstock such as wood chips or agricultural waste [1]. However, the diversity in sources often leads to variable proportions of H_2 and CO, along with the inclusion of other hydrocarbons in syngas such as CH_4, and inert species such as H_2O and CO_2 [2]. This variability in fuel composition can significantly affect the combustion process of syngas, specifically diffusive-thermal instabilities (DTIs) which are the focus of this work.

DTIs are intrinsic combustion phenomena that result from unequal thermal and molecular diffusivities, and that generally lead to cellular or pulsating flames [3]. DTIs are favored at high dilution levels [4], which render them relevant to many low-emission combustors, including burners in biomass conversion systems that typically feed on low calorific value syngas [5]. DTIs also play a key role in the extinction/re-ignition dynamics of non-premixed flames [6], and therefore, pollutant formation of locally quenched flames interacting with the walls of compression ignition engines or gas turbines [7]. While fundamental studies on DTIs have been mostly conducted using idealized laminar flames due to their inherent simplicity, as discussed next, the effect of DTIs on real flames with much higher strain rates and shorter residence times remain significant. Yang et al. [8] demonstrated that in the wrinkled and corrugated flamelets turbulent regimes, intrinsic cellular instabilities significantly modify the propagation characteristics of the turbulent flame. Also, DTIs that scale with the flame thickness are often filtered out by Large Eddy Simulations of turbulent combustion which exhibit desperate scales [9]. A proper description of these small-scale cells could be incorporated into the sub-grid models for improved accuracy without compromising computational efficiency.

DTIs have been reported in both premixed and non-premixed flames [6] using various fuels. However, when it comes to syngas, the majority

* Corresponding author.
E-mail address: elie.antar@polymtl.ca (E. Antar).

https://doi.org/10.1016/j.combustflame.2024.113313
Received 29 June 2023; Received in revised form 9 January 2024; Accepted 9 January 2024
Available online 16 January 2024

Nomenclature

$\mathfrak{B}$:	Arrhenius pre-exponential factor (m^3/mol s)
c_p:	Specific heat at constant pressure (J/kg K)
D_a:	Damköhler number (-)
D_{th}:	Thermal diffusivity (m^2/s)
DTI:	Diffusive-thermal instability
E:	Activation energy (J/mol)
f:	Pulsation frequency (1/s)
l_D:	Diffusion length (m)
L:	Length of the one-dimensional combustion zone (m)
Le_i:	Lewis number of species i (-)
$Le_{F,eff}$:	Effective fuel Lewis number (-)
N_{cells}:	Number of cells (-)
p_0:	Ambient pressure (Pa)
q:	Heat release per unit mass of fuel (J/kg)
R:	Ideal gas constant (J/kg mol)
T_a:	Adiabatic flame temperature (K)
U:	Bulk velocity (m/s)
$\overline{W}$:	Mean molecular weight (kg/kmol)
x_f:	Normalized flame position (-)
X_{H_2O}:	Molar fraction of H_2O relative to CO_2 (-)
X_i:	Molar fraction of species $i = \{H_2, CO, CH_4\}$ relative to the other combustible species in the fuel stream (-)
X_F:	Total fuel concentration (-)
λ:	Thermal conductivity (W/m K)
λ_c:	Cell size (mm)
ν_i:	Stoichiometric coefficient of species i
σ^*:	Instability wavenumber (-)
ϕ:	Initial mixture strength (-)

of the published studies rely on premixed configurations such as flat flame McKenna [10,11] or Bunsen burners [12,13], as well as spherically expanding flames [14,15], in which aerodynamic effects have a significant influence on the flame. The instabilities reported are often a combination of hydrodynamic, buoyancy, and diffusive-thermal effects, and are mainly wrinkled flames, with scarce reference to any potential DTI pulsations from CH_4, CO, or any other large Lewis number species, which could lead to extinction.

As a result, to diminish the parasitic hydrodynamic effects and put the spotlight on DTIs, we aim to experimentally replicate the idealized one-dimensional chambered diffusion flame configuration. This approach was first introduced by Kirkby and Schmitz [16] as a theoretical construct, and is shown in Fig. 1. The fuel is assumed to be supplied at a constant velocity via a semi-permeable membrane into the bottom of the straight-duct combustion chamber, which is exposed to constant conditions at the top. The latter are ensured by a sufficiently fast flowing transverse stream that uniformly removes the combustion products and supplies the oxidizing species, which counter-diffuses towards the flame against the bulk flow. Therefore, given that the flow is uniform throughout the combustion chamber in this theoretical construct, the resulting flame is unstrained.

Due to its simplicity, the idealized one-dimensional configuration

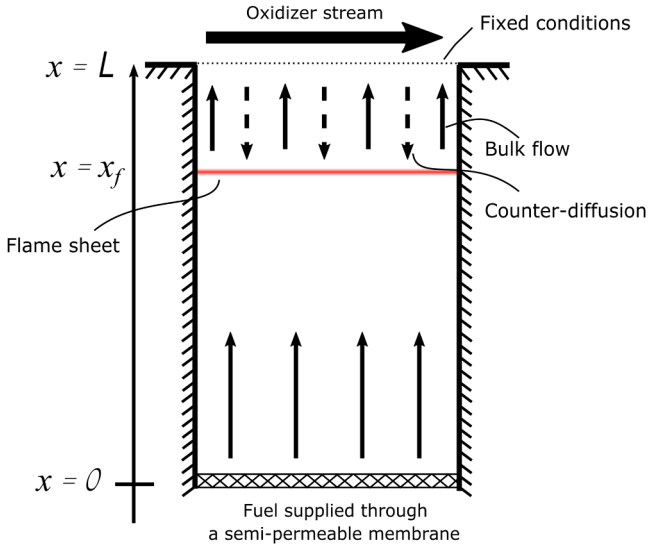

Fig. 1. The idealized one-dimensional chambered diffusion flame theoretical construct.

has been previously used to develop DTIs models, such as the theoretical work of Metzener and Matalon [17]. Their linear stability analysis showed that DTIs arise when preferential diffusion of mass or heat (non-unity and unequal Lewis numbers) lead to excess or deficiency in available enthalpy ($h_f \neq 0$) at the flame sheet with a Damköhler number (D_a) below a critical value (D_a^*). D_a is the ratio of the characteristic diffusion time over the chemical reaction time. Unlike premixed flames where a single effective Lewis number is sufficient to predict the characteristics of the DTIs, it was shown that both the fuel and oxidizer Lewis numbers (Le_F and Le_o) must be considered in diffusion flames. Fundamental scaling laws were also obtained for different instability parameters such as cell size or pulsation frequency.

In a later study, [18] it was also demonstrated that unlike in premixed flames, the ubiquitous hydrodynamic effects from thermal expansion play a secondary role in the stability of diffusion flames, with diffusive-thermal effects being the main protagonist. A constant-density linear stability analysis of the one-dimensional diffusion flame was compared to a case where thermal expansion was taken into account, and qualitative agreement in terms of the predicted instability types was obtained. The Lewis number maps of the different instability patterns were similar, highlighting the major role played by diffusive-thermal effects in diffusion flames, which further motivates their use in the current study.

The introduction of an experimental implementation that can mimic the idealized one-dimensional diffusion flame by Lo Jacono et al. [19] (mark I unstrained burner), which was subsequently enhanced by Robert and Monkewitz [20] (mark II unstrained burner) has enabled DTI theoretical models to be validated for the first time against experimental data obtained in essentially unstrained conditions [21]. The planar flames generated were estimated to have a residual strain rate as low as $0.05s^{-1}$. The characteristics of the stationary cells in the small Lewis number H_2-CO_2 flames, and the pulsating instabilities of the CH_4-CO_2 flames with a relatively larger Lewis number were in agreement with theoretical predictions.

Despite the numerous fundamental studies on DTIs over the past decades, the focus was mainly on single-reactant fuels such as H_2 or CH_4. The characteristics of the instabilities in multi-fuel mixtures such as syngas are different, whereby we recently showed [22] that the combined presence of H_2 with a high diffusivity, and CO/CH_4 with much lower mobility could result in superimposed cellular-pulsating flames. Despite the novel insight, only CO_2 was used for dilution in the aforementioned study, since the mark II version of the unstrained diffusion flame burner was limited to dry gaseous fuels. With distinctive diffusive-thermal properties, the effect of H_2O on the instability type and size in syngas remains unknown, and cannot be reliably predicted by existing theoretical models as they are based on single-reactant fuels.

Therefore, a modified burner design that is compatible with vaporized fuel mixtures, and more experimental data are needed to gain a deeper understanding of the peculiar instabilities that form in multi-fuel flames.

H_2O is a major diluent in biomass-derived syngas in addition to CO_2, and our recent model of a small-scale biorefinery [5] predicts that its total concentration could reach 70% in some cases before the combustion stage. H_2O leads to non-trivial dilution effects, whereby higher flame temperatures are attained relative to CO_2 dilution, however, with an increased risk of extinction due to chemical effects [23]. Although H_2O can be readily condensed from syngas mixtures in biorefineries, we showed in [5] that a 35 percentage point total efficiency penalty could be incurred by cooling the gas to atmospheric conditions to condense the water. In fact, adopting hot gas handling techniques where thermal energy losses are reduced plays a key role in enhancing the economic viability of biomass conversion systems [24], especially for small-scale decentralized applications that are inherently well suited to the distributed nature of biomass resources. In addition, burning with steam at lower flame temperatures is often favored in different practical combustors to reduce NO_x emission [25], soot formation [26], and radiative heat losses [27].

The goal of this paper is to introduce a new version (mark III) of the unstrained diffusion burner that can be operated with wet gaseous fuels, and utilize this research facility to investigate DTIs in H_2O-diluted H_2-CO-CH_4-CO_2 mixtures. In the subsequent sections, the design of the burner is discussed, followed by a characterization of its ability to produce unstrained diffusion flames through comparison with an idealized one-dimensional flame model. This is followed by results covering the stability and extinction limits of a broad range of humid syngas mixtures, before characterizing the instabilities that form beyond the marginal stability limit, with a strong emphasis on the effect of H_2O dilution.

2. Unstrained diffusion flame burner

2.1. Mark III design

Fig. 2 shows a schematic representation of the mark III version of the one-dimensional unstrained diffusion flame burner. The combustion chamber is a straight quartz glass duct with a 77.5 × 77.5 mm cross section and a length of 53.8 mm (L_{geom}), and is supplied from the bottom with fuel at a constant bulk velocity and at nearly atmospheric pressure. The oxidizer stream (pure O_2) is fed from the top, with O_2 counter-diffusing downwards against the combustion products to reach the flame. The flow rates of the gasses are controlled using flow controllers (Hastings, model HFC-202).

Similar to the mark II version of the burner, the conditions at the top of the chamber are kept constant by supplying the oxidizer stream using 31 × 31 hypodermic needles (ID: 0.8 mm), and allowing the products to evacuate via an interlaced set of 32 × 32 thin curved stainless steel tubes that are exposed to atmospheric pressure at the outlet. The needles array is placed inside an insulated plenum, which is fitted with heaters and thermocouples to control the top boundary temperature of the combustion zone and to avoid condensation within the exhaust stream. To shield the central part of the flame where the experiments are conducted from the temperature and species gradients of the colder windows, a 1 mm thick quartz cylinder with a 43.5 mm inner diameter is inserted in the middle of the combustion chamber. This divides the flame into a pilot outer portion that shields the inner planar flame from the windows, where the measurements are taken, as shown in Fig. 2c).

Particle Image Velocimetry (PIV) reported in [28] revealed that the nature of the oxidant supply into the combustion chamber creates a thin layer below the top needles array in which the flow is locally three-dimensional, and where a portion of the supplied oxidizing species is directly evacuated upwards with the combustion products. This injection layer is represented schematically in Fig. 2b), and was

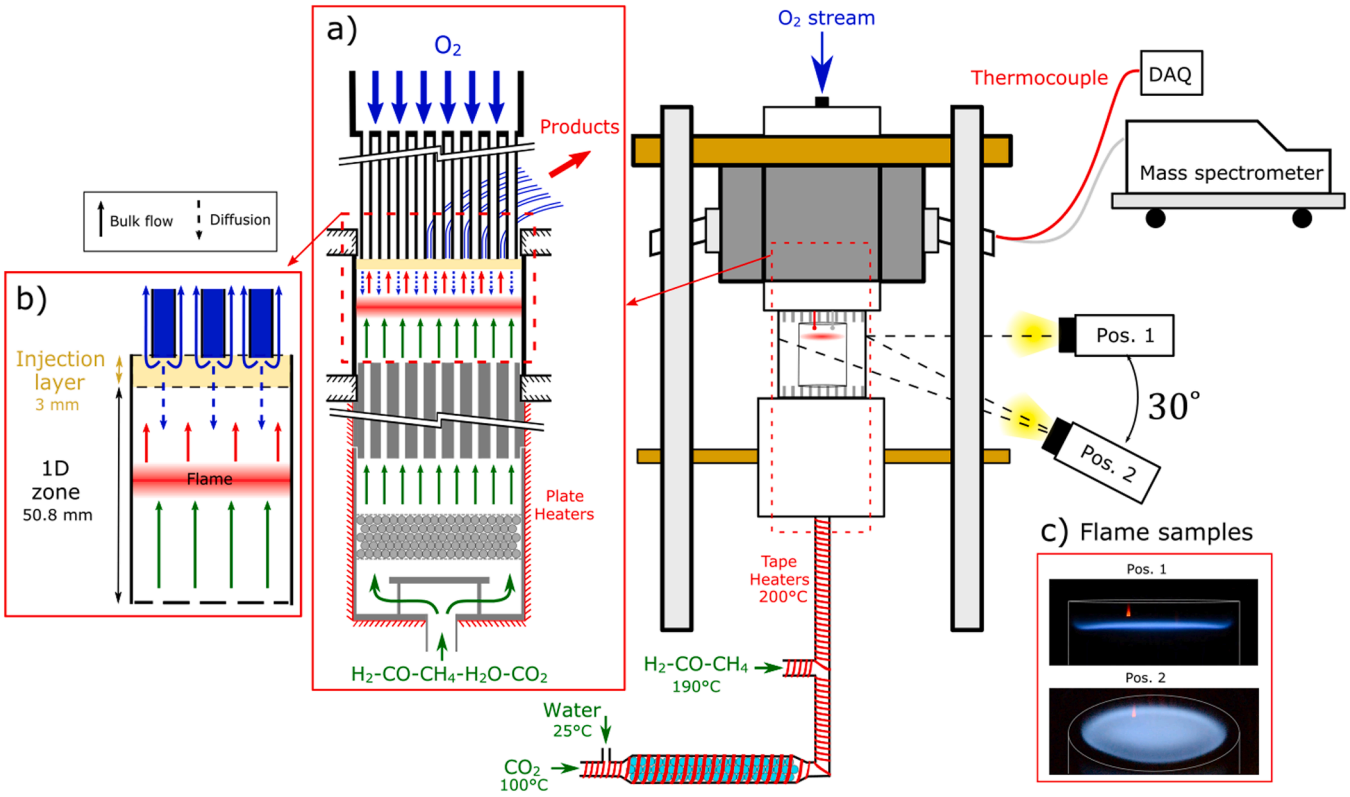

Fig. 2. Schematic representation of the mark III unstrained diffusion flame burner. Cross-sectional views showing a) the reactants injection and exhaust systems, and b) the injection layer and the one-dimensional combustion zone. c) Flame samples captured from positions 1 and 2.

conservatively measured to have a thickness (Δ) below 3.0 mm using laser Doppler anemometry (LDA) [29]. Below the injection layer, species concentration becomes highly uniform across the combustion chamber, as revealed by mass spectrometer measurements, where variations in O_2 concentration just below 10% were limited to the region near the inner cylinder due to the inevitable wall effects [28,29]. Consequently, this led the temperature across the central part of the flame to agree to within 3% with the adiabatic solution. Therefore, the effective combustion chamber length that mimics the idealized one-dimensional chambered diffusion flame configuration is $L = L_{geom} - \Delta = 53.8 - 3 = 50.8$ mm.

Due to the mixing that happens in the injection layer, the oxidizer boundary of the one-dimensional zone is diluted with CO_2 and H_2O. The species concentration at this location is measured using a mass spectrometer, calibrated for major species (H_2, O_2, CO_2 and H_2O) at a relative accuracy of 5%, which is estimated to increase to 10% if inserted in the flame sheet itself due to the relatively higher concentration of radicals [30]. The gas is sampled using a fused silica capillary with a 0.1 mm internal diameter and an extraction flow rate of 0.2 mL/min. The capillary is inserted into the combustion chamber via the top needles array and sheathed in a thin stainless steel capillary with a 0.4 mm outer diameter. For a given flame, the sampling is stopped only after obtaining a steady signal, which typically required a few minutes. The whole sampling line is heated to 180°C to prevent condensation, and the position of the probe is precisely controlled by a micrometer, and verified optically from outside the chamber.

The main difference between the current and the mark II version [28] of the unstrained diffusion flame burner is the former's ability to operate with fuels having a very high vapor content. As a result, the fuel injection system had to be redesigned. As illustrated in Fig. 2a), an aluminum injection chamber (81-mm long) is used, which is uniformly heated by 76-mm long plate heaters from the sides and the bottom. On the top, a 36-mm thick aluminum block is placed and sealed by gaskets, through which an array of 18 × 18 2-mm diameter holes are made to uniformly supply the fuel into the combustion chamber at 142°C. This block is also uniformly heated from all sides using four PID-controlled plate heaters. The temperature variation across the outlet of the fuel injection block was measured to be less than 2°C, using multispectral-infrared camera (Telops MS-350) as shown in Fig. 3a).

To add humidity to the fuel stream, a syringe pump feeds water to a CO_2 carrier stream at 100°C, which is circulated through a 20-cm long tube heated to 200°C and filled with 1-mm glass beads, for uniform evaporation, before being mixed with the remainder of the hot fuel stream of H_2/CO/CH_4 upstream of the injection chamber. Mass spectrometer measurements inside the injection chamber are shown in Fig. 3b), using a binary CO_2-H_2O mixture for illustration. The four jumps represent the transient phase when the flowrates and hence, the proportions of the gasses change. After these transient periods lasting on the order of one minute, it can be seen that the water vaporization and mixing processes are steady.

2.2. *Burner characterization - stable flames*

Fig. 4a) shows the structure of a stable H_2 flame generated in the mark III burner, and compares it with the idealized one-dimensional diffusion flame solution at an initial mixture strength of $\phi = 0.5$. The latter is defined as the ratio of the fuel to oxygen boundary mass fractions, normalized by their stoichiometric proportions. Consequently, ϕ can be considered as an equivalence ratio based on the supply conditions, as stoichiometry is always respected at the flame sheet in diffusion flames. Strong agreement between the produced flame and the idealized

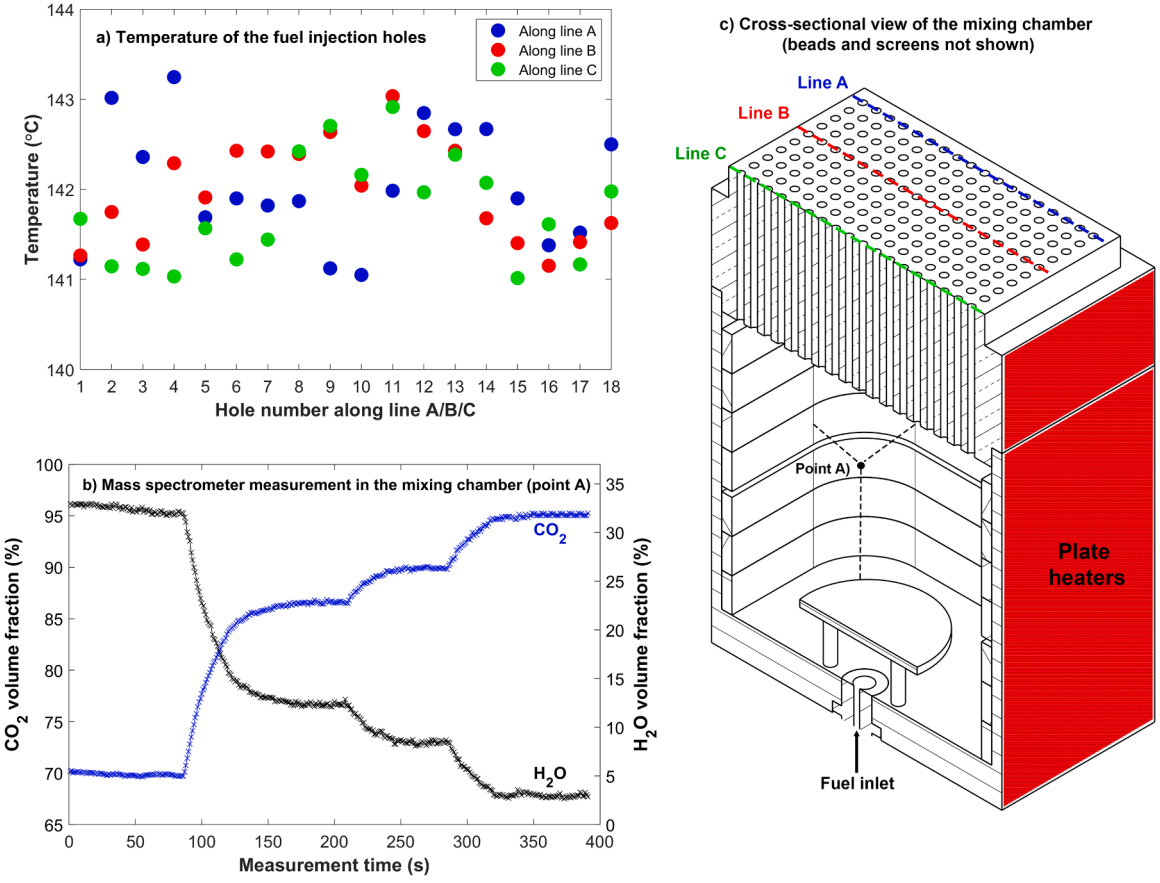

Fig. 3. a) Temperature of the fuel injection block holes, and b) temporal variation of the gasses volume fraction within the mixing chamber. A cross-sectional view of the latter is shown in c).

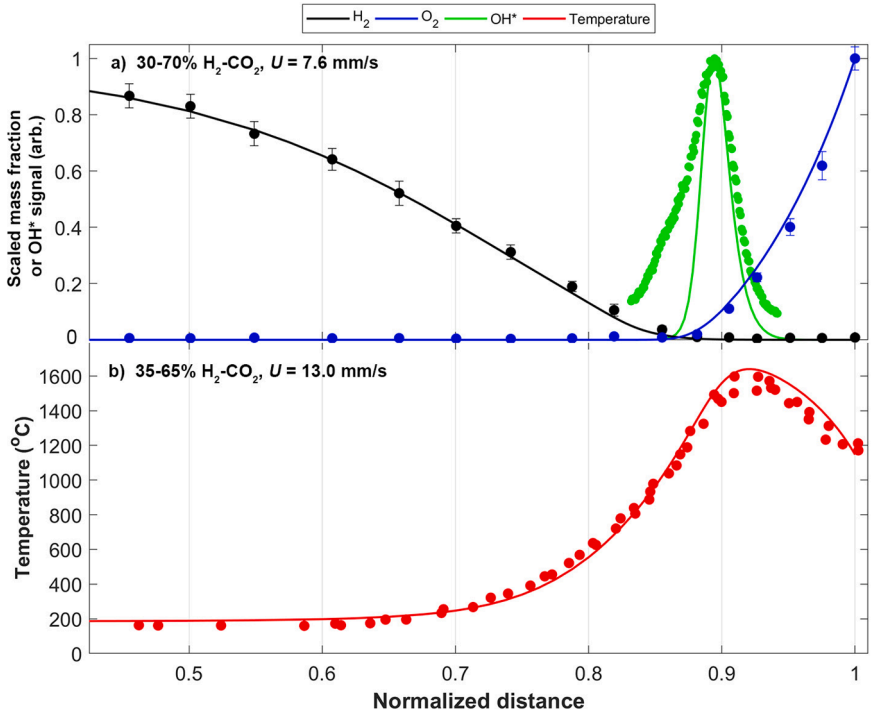

Fig. 4. a) Structure of a H_2 flame diluted with 70% CO_2 at $\phi = 0.5$ and $U = 7.6$ mm/s evaluated at the inlet conditions. b) Temperature profile of a H_2 flame with 65% CO_2, $\phi = 0.5$ and $U = 13$ mm/s in the mark II burner, highlighting very small heat loss effects. (○): Experimental data, and (—): one-dimensional diffusion flame model.

solution can be seen in terms of the flame position, and major reactants mass fraction profiles, which are scaled by their respective boundary concentrations. The distance along the combustion chamber is normalized by its length.

The idealized diffusion flame solution is implemented on Python using Cantera software package [31]. The flame is modelled as a stack (Sim1D) containing from left to right an inlet of the advected flow (Inlet1D), an adiabatic one-dimensional flow field (UnstrainedFlow), and an outlet reservoir with constant boundary conditions (OutletReservoir1D). The steady one-dimensional finite-difference momentum, energy, species and overall continuity equations are solved by the Cantera solver, which uses a hybrid Newton's method and time-stepping scheme for convergence, along with adaptive grid refinement, as detailed in [31]. The flow is assumed to be an ideal gas mixture, while taking into account Soret diffusion effects, and using the GRI-3.0 reaction mechanism. This one-dimensional diffusion flame model has been used and validated previously in various works [21,22,28].

In Fig. 4b), the temperature profile of a H_2 flame in the mark II burner [28], which adopts a similar quartz combustion chamber as in the mark III burner, shows strong agreement with the idealized one-dimensional diffusion flame model. This shows that radiation heat loss effects do not play a significant role in such configurations, unlike in an open flame, as here the combustion chamber is completely enclosed and the burner is well insulated, except for windows for optical access.

Analytical treatment [20] dictates that the position of a stable one-dimensional diffusion flame is a function of $\widetilde{U}$, Le_F, Le_o, and ϕ, with

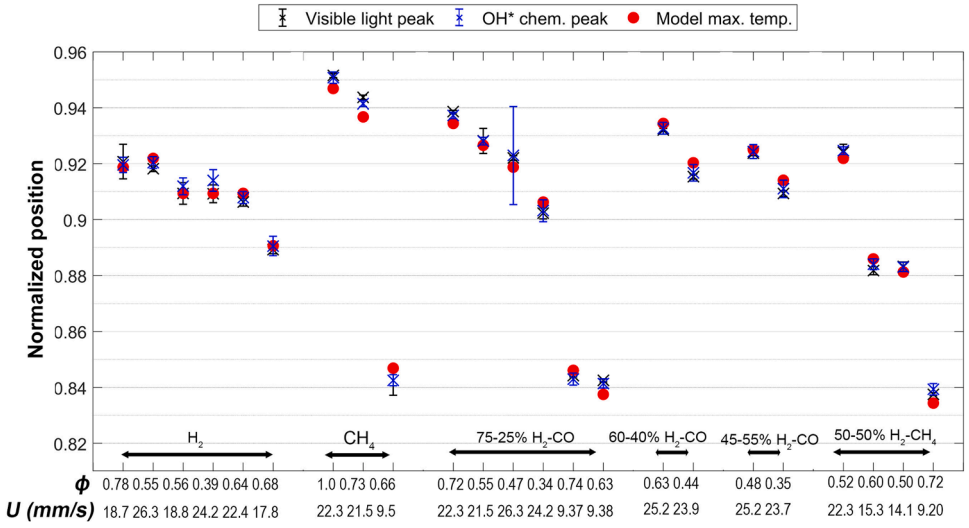

Fig. 5. Comparison between experimental and modelled flame positions under different conditions.

$\widetilde{U}$ being the non-dimensional bulk velocity $\widetilde{U} = U/(D_{th}/L)$. Given that $\widetilde{U}$ is affected by the flame temperature, we use the flame position in Fig. 5 as another proxy to demonstrate the general agreement between flames generated in our burner and idealized one-dimensional diffusion flames. The positions of the maximum visible light and OH* chemiluminescence signals are compared with the location of the maximum temperature from the idealized model for a range of fuel blends, initial mixture strengths, and inlet bulk velocities. The error bars in the experimental measurements represent the reproducibility of the results through their minimum and maximum values, and the acquired noise that is amplified by the image intensifier. The OH* chemiluminescence measurements are conducted using a 310-nm optical filter (10 nm bandwidth), a UV lens, an image intensifier (UVi model 1850–10), and a high-speed camera (Photron AX-200). The latter is placed perpendicular to the burner axis as shown in Fig. 2 (Pos. 1). The light signals are normalized by their peak values, and averaged laterally over the flat flame surface, along with temporally over multiple images to reduce noise.

As can be seen from Fig. 5, the flames studied were limited to $x_f > 0.8$, to avoid buoyancy–driven Rayleigh–Bernard convection cells that could arise from the temperature stratification in the fluid layer between the flame and the colder top boundary. These instabilities onset when the dimensionless Rayleigh number (Ra) is above a critical value, 1708 for a fluid layer sandwiched between rigid boundaries, and 657.5 for free boundaries according to analytical predictions [32]. Given $Ra \sim (1-x_f)^3$ [29], we made sure that the flame is positioned sufficiently high in the chamber to avoid these undesirable effects, where it is estimated that $Ra < 400$. Upon their onset, buoyancy-driven instabilities were easily distinguishable through the dramatic flame curvature that they caused. They are distinctively larger in size and amplitude compared to the stationary cells induced by diffusive-thermal instabilities, and always grew unsustainably with time, causing the flame to collapse on the bottom needles array of the burner. A visual illustration of Rayleigh–Bernard convection cells forming in the mark II burner is provided in the supplementary material of our earlier work [22].

2.3. Burner characterization - stability and extinction limits

Fig. 6a) presents the stability limits of different syngas fuel blends, with emphasis on 75–25% and 60–40 H_2-CO% ratios, as these are typically encountered in biomass-derived syngas [5]. The total fuel concentration (X_F) is defined as:

$$X_F = \dot{N}_{H_2} + \frac{\dot{N}_{CO} + \dot{N}_{CH_4}}{\dot{N}_{H_2} + \dot{N}_{CO} + \dot{N}_{CH_4} + \dot{N}_{H_2O} + \dot{N}_{CO_2}} \quad (1)$$

with $\dot{N}_i$ being the molar flow rate of species i in the fuel stream. For a given fuel blend, the total fuel concentration of a stable planar flame is gradually reduced in $X_F = 0.25\%$ decrements until the first instability is observed in the flame. The initial mixture strength is kept on average at $\phi = 0.58$, by controlling the flow rate of the oxidizer stream. The inlet bulk velocity is fixed at $U = 11$ mm/s for the results presented. The fuel species notation first indicates the volume fraction of H_2 relative to CO, followed by the fraction of CH_4 relative to the two other combustible species. For the two inert species, the H_2O molar fraction relative to CO_2 (X_{H_2O}) is indicated:

$$X_{H_2O} = \frac{\dot{N}_{H_2O}}{\dot{N}_{H_2O} + \dot{N}_{CO_2}} \quad (2)$$

For instance, a 75–25% H_2—CO + 15% CH_4 mixture diluted at $X_F = 30\%$ with $X_{H_2O} = 20\%$ is composed of a tertiary fuel containing 85% H_2+CO at a relative ratio of 0.75 and 0.25, and 15% CH_4, and a binary diluent containing CO_2+H_2O at a ratio of 0.8–0.2. The fuel to diluent ratio is 0.3–0.7, yielding a global reaction for the combustion of 100 mol of this fuel mixture:

$$19.1H_2 + 6.4CO + 4.5CH_4 + 21.75O_2 \rightarrow 10.9CO_2 + 28.1H_2O \quad (3)$$

Data on the stability limits of syngas are scare in the literature, and the results of Fig. 6a) show that replacing CO_2 with H_2O for the same total fuel concentration renders the flame more susceptible to instabilities, for the broad range of fuels considered. For instance, with 75–25% H_2-CO + 15% CH_4, instabilities are first observed at $X_F = 21.0\%$ when the mixture is dry. However, as water replaces 20% of the CO_2 by volume, instabilities onset at $X_F = 23.0\%$, which becomes $X_F = 24.75\%$ at $X_{H_2O} = 40\%$. Comparing different fuel blends at a given X_{H_2O}, the measured stability limits show that the flame becomes most prone to instabilities when the CO content in the fuel mixture is increased. For instance, as CO is increased from 75 to 25% H_2-CO to 60–40% H_2-CO at $X_{H_2O} = 40\%$, the fuel concentration at which instabilities onset increases from $X_F = 25.25\%$ to 26.0%. At 45–55% H_2-CO, instabilities are observed at $X_F = 26.75\%$. In addition, the results show that flame stability is enhanced when the CH_4 content in the fuel is increased. As 15%

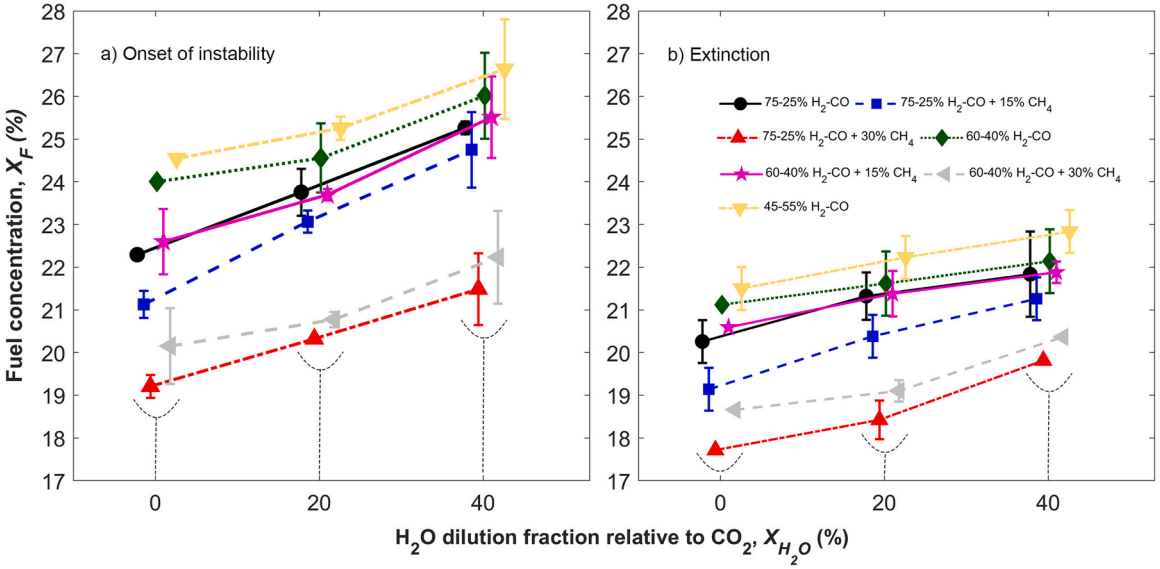

Fig. 6. Flame a) stability and b) extinction limits as a function of the water dilution fraction for different fuel blends. The inlet bulk velocity is $U = 11$ mm/s. The error bars indicate maximum variation in the measurements, and in a) account for the deviation of the initial mixture strength from its mean value of $\phi = 0.58$.

CH_4 is added to a mixture of 60–40% H_2-CO with $X_{H_2O} = 20\%$, the onset of instability is delayed from $X_F = 24.75\%$ to $X_F = 23.75\%$. When 30% CH_4 is added, the stability limit is further pushed to $X_F = 20.75\%$. The characteristics of the instabilities are discussed in detail in the next sections.

Fig. 6b) shows the dilution-induced extinction limits, which are fuel concentrations below which no flame could be maintained. Here, the combustion is excessively weak, whereby the chemical reaction time is very large relative to the residence time. The instabilities that develop are always unsustainable and rapidly extinguish the flame, no matter the boundary oxygen concentration or initial mixture strength. Experimental data on the extinction limits of syngas diffusion flames are scarce, and numerical studies often consider a limited range of syngas composition. The data presented herein for a broad ranges of syngas mixtures could be useful for flamelet modelling of turbulent non-premixed flames, which could be represented by an ensemble of laminar diffusion flamelets with a one-dimensional inner structure [33].

As shown in Fig. 6b), the extinction limit trends are similar to the stability limits, where it can be seen that higher H_2O volume fractions relative to CO_2 render the flame more prone to extinction, for all fuel blends. To explain this behaviour, we dissect the different dilution effects, i.e. inert, thermal/diffusion, and chemical effects, by introducing four artificial species (XH_2, XCO, XCO_2, and XH_2O) into the chemical reaction mechanism of our one-dimensional flame model, similar to the approach by Shih and Hsu [34]. The artificial species are chemically inert, but have the same physical properties as their counterparts, and 75–25% H_2-CO fuel is used for demonstration. The inert effect simply highlights the consequences of the reduction in the reactants concentration, by assuming that the diluents are chemically inert, and have the same thermal and diffusive properties as the fuel. Consequently, the mixture is diluted with 75–25% XH_2-XCO, yielding a $X_F = 16.75\%$ extinction limit, as can be seen from Fig. 7.

The thermal/diffusive effect, hereafter referred to as thermal, illustrates the consequences of changing the thermal and transport properties of the diluted mixture. For these purposes, a chemically inert XCO_2-XH_2O diluent is used, with a composition equivalent to X_{H_2O}. From Fig. 7, it can be seen that the thermal effect promotes extinction at all X_{H_2O} considered, and this can be attributed to the fact that both diluting species have higher volumetric heat capacities compared to the fuel species, leading to lower flame temperatures. For instance at 1227°C, $c_{p,CO_2} = 58.3$ kJ/kmol.K, and $c_{p,H_2O} = 51.4$ kJ/kmol.K, while $c_{p,H_2} = 32.0$ kJ/kmol.K and $c_{p,CO} = 35.2$ kJ/kmol.K.

While it can also be seen that from a thermal effects point of view, replacing CO_2 with H_2O tends to delay extinction to lower fuel concentrations ($c_{p,H_2O} < c_{p,CO_2}$), this is outweighed by the enhanced chemical effects at higher water fractions, which overall, promotes extinction as shown in Fig. 7. Such H_2O/CO_2 dilution effects are consistent with the numerical simulations of Shih et al. [23] in low-strain 50–50% H_2-CO diffusion flames, but to our knowledge, are confirmed experimentally for the first time in this work for different syngas mixtures. As detailed in [34], water vapor addition increases the OH radical pool, which on one part favors the main exothermic reactions: $OH + H + M \rightarrow H_2O + M$ (R43 in GRI-3.0), $H_2 + OH \rightarrow H_2O + H$ (R84), $CO + OH \rightarrow CO_2 + H$ (R99), and $OH + HO_2 \rightarrow O_2 + H_2O$ (R287), which happen to be however, either chain terminating (ex: R43 and R287) or H_2O/CO_2-producing (R84 and R99) reactions. Consequently, H_2O dilution leads to flames with higher temperatures, which nonetheless extinguish at higher fuel concentrations as shown in Fig. 7.

3. Diffusive-thermal instabilities

The characteristics of the diffusive-thermal instabilities that are observed beyond the stability limits are presented next. We start by discussing the effect of water dilution on the instability type in subSection 3.1, followed by its effect on the characteristic length and time scales in subSection 3.2. For a given fuel, the diluent composition is fixed through X_{H_2O}, and the total fuel concentration is gradually decreased, going through marginal stability where DTIs first onset, towards the extinction limit. For every state, the flame properties are extracted, and the instability characteristics are reported as a function of the Damköhler number, initial mixture strength, and fuel and oxidizer Lewis numbers. Dispersion relations derived by linear stability analysis of unstrained diffusion flames [35] are a function of these four parameters, in addition to the temperature difference between the two boundaries (ΔT). Given its relatively minor influence compared to the other parameters, ΔT is kept approximately constant in our experiments at $\Delta T =$ 700°C using the plenum heaters.

Given that we are dealing with fuel mixtures, an effective Lewis number ($Le_{F,eff}$) for the fuel mixture is considered:

$$Le_{F,eff} = X_{H_2} Le_{H_2} + X_{CO} Le_{CO} + X_{CH_4} Le_{CH_4} \quad (4)$$

where the Lewis number of each fuel species (Le_i) is weighted with its relative fraction in the fuel stream (X_i). The Lewis numbers of each fuel species, along with that of the oxidizer, are calculated at the flame sheet using the one-dimensional diffusion flame numerical model supplied with experimentally-measured boundary conditions. The molecular diffusivity used in the computation of Le_i is a mixture-average one, since the highly-diluted flames studied here are abundant in both CO_2 and H_2O. The initial mixture strength is calculated from the boundary conditions measured using the mass spectrometer, and the Damköhler

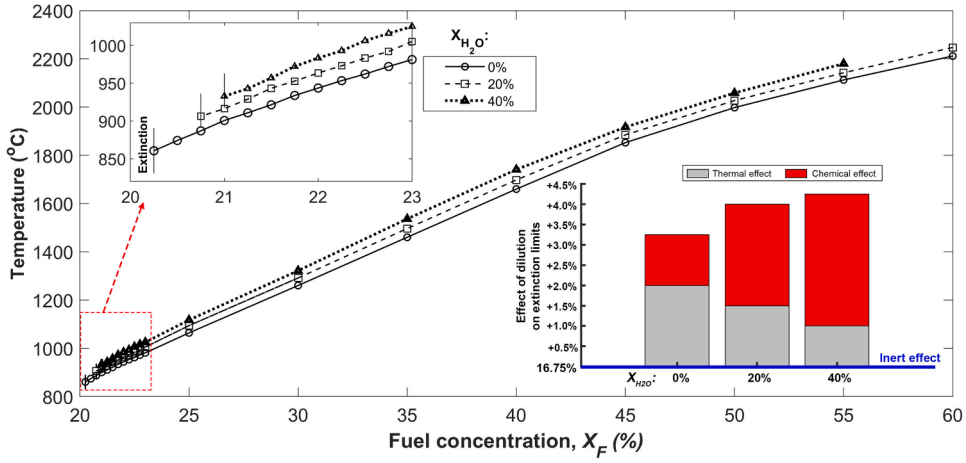

Fig. 7. Variation in flame temperature with fuel concentration at different water fractions, and dilution effects analysis for a 75–25% H_2-CO mixture at $\phi = 0.5$ and $U = 11$ mm/s.

number is estimated as per the following equation:

$$D_a = \left(\lambda/\rho_a c_p U^2\right)\left(R^0 T_a/E\right)^3 \left(\nu_x c_p \overline{W}/qR^0 W_f\right)\mathfrak{B} Y_{f,o} p_0 \exp(-E/RT_a) \quad (5)$$

where the values of the activation energy E and the Arrhenius pre-exponential factor $\mathfrak{B}$ are assumed constant for a given fuel blend, owing to the lack of suitable empirical data. The values for these two parameters are selected such that Damköhler number at the marginal stability state for a given fuel blend is equal to unity [21,22]. This means that the D_a calculated in this paper is a relative one, with respect to the marginal stability: $D_a = D_{a,actual}/D_a^*$.

3.1. Effect of H_2O dilution on the instability type

For completeness, we first show the instabilities that are promoted by each of the three fuel species individually in Fig. 8. These maps are generated by gradually reducing the fuel concentration of a strongly burning flame down to the extinction limit, going through the marginal stability state where instabilities are first observed. This is conducted at bulk velocities that vary between $U = 8$ and 24 mm/s (calculated at the inlet), to maximize the mapped Damköhler number space for each fuel.

Starting with the H_2 flames at $X_{H_2O} = 0$ and 40%, travelling waves are the first pattern observed at both X_{H_2O} in the vicinity of the marginal stability state ($D_a = 1$, by definition). These instabilities involve cells that vary in number between 4 and 5, corresponding to a cell size between 18.5 and 29.7 mm, and that rotate around the central axis at approximately 3 Hz. Details on the optical diagnostics used to measure the instabilities can be found in [22]. This mixed cellular-rotation instability mode, which is sometimes referred to as oscillatory cells, is shown in Fig. 9a), where the images are taken using a digital still camera (Nikon D5300) with a 30° upward angle (Position 2 in Fig. 2). At lower Damköhler numbers, the rotation stops and holes appear for the first time in the flame sheet, turning it partly cellular, as shown in Fig. 9b). Fuel is detected to escape through these holes, as revealed by the mass spectrometer measurements shown in Fig. 9d), where the sampling probe was placed above the hole that forms in the flame. The degree of cellularity keeps increasing as the Damköhler number is further reduced, where fully cellular flames form with stationary cells that vary in number and spacing between 12 and 17 and 8–10 mm, respectively, as shown in Fig. 9c). Unlike partly cellular flames, fully cellular instabilities involve cells that are completely detached from their neighbours, and that take on a similar circular shape. Fuel leakage between the cells considerably increases near the extinction limit, a behaviour which was also predicted by theoretical models [36].

The behavior of H_2 flames is consistent with the results from the linear stability theory [36], as was also reported in our experiments with the mark II version of the burner [22] using dry H_2 flames. As shown in the Lewis number map of Fig. 10, at relatively large D_a, Le_{H_2} is located outside the theoretical stationary cells zone and below the planar intensity pulsations zone. Under such conditions, mixed instability modes such as travelling waves are predicted. However, as D_a decreases, the region where stationary cells onset expands, and eventually engulfs the Lewis numbers of our H_2 flames. Such a behaviour is observed for all X_{H_2O} tested ($0\% \leq X_{H_2O} \leq 40\%$). However, as can be seen in Fig. 8, the transition from travelling waves into partial and then full cellularity is delayed to lower Damköhler numbers relative to the marginal stability state, as the water fraction is increased. This is because the Lewis numbers of both H_2 and O_2 increase from 0.22 to 0.88 to 0.27 and 1.0, respectively, as H_2O replaces 40% CO_2 by volume, as shown in Fig. 10.

Fig. 8 also presents the instabilities of CO and CH_4 flames at various Damköhler numbers. The initial mixture strength is varied between $\phi = 0.5$ and 3, and X_{H_2O} between 0 and 40%, although for CO, a minimum of $X_{H_2O} = 10\%$ is maintained as pure-CO flames were never sustainable, as also reported in [23]. As indicated by the solid circular symbols, only planar intensity pulsations with no cellular instabilities form for these fuels for the wide range of conditions tested. An illustration of the typical periodic variation in flame position resulting from planar intensity pulsations is shown in Fig. 11 for CO and CH_4. The observed instabilities is again consistent with previous experimental work [21,22], and with the theoretical stability map of Fig. 10, where pulsations are predicted for high fuel and oxidizer Lewis numbers. The CO pulsation frequency varies between 0.7–1.2 Hz, and is lower than that of CH_4 at 1.2–2.0 Hz. Besides the nature of the fuel, the pulsation frequency also depends on the operating conditions, particularly the fraction of water

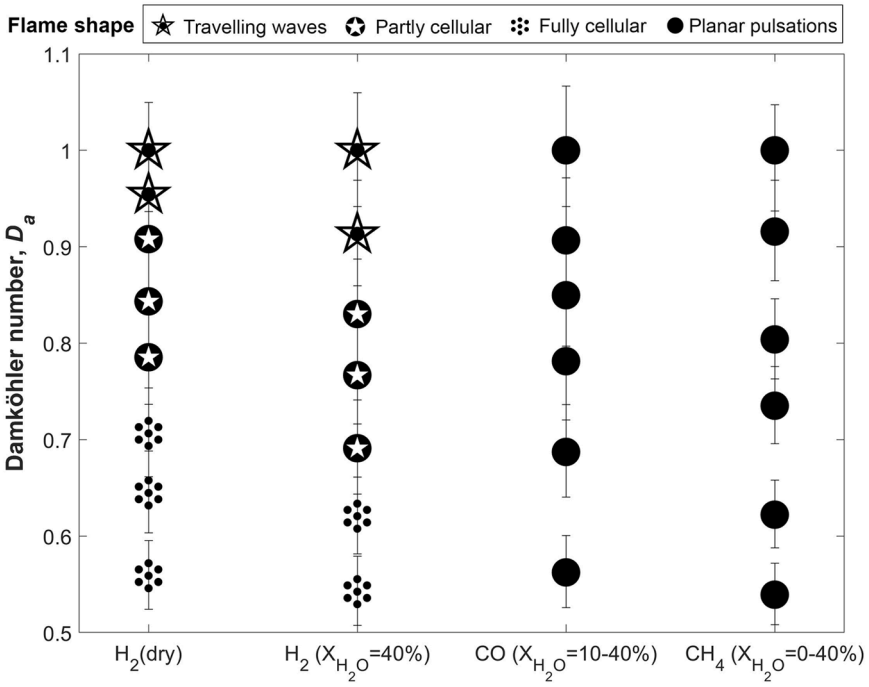

Fig. 8. Flame instability patterns of single-fuel H_2, CO and CH_4 mixtures diluted in H_2O and CO_2. The initial mixture strength is kept approximately constant at 0.4 for H_2 ($X_{H_2O} = 0$ and 40%), and varies between 0.5 and 3.0 for the CO and CH_4 flames.

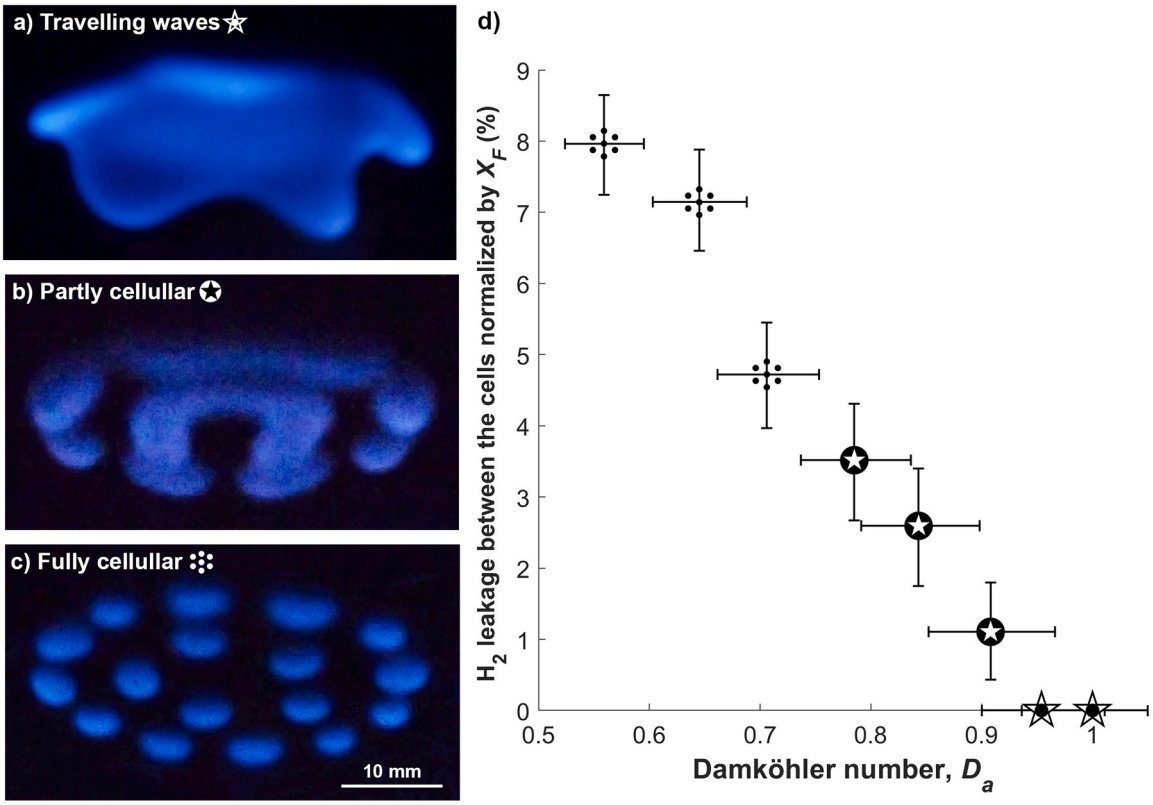

Fig. 9. a) Travelling waves, b) partly cellular, and c) fully cellular H_2 flames at $\phi \approx 0.4$. d) Mole fraction of leaked H_2 between the cells.

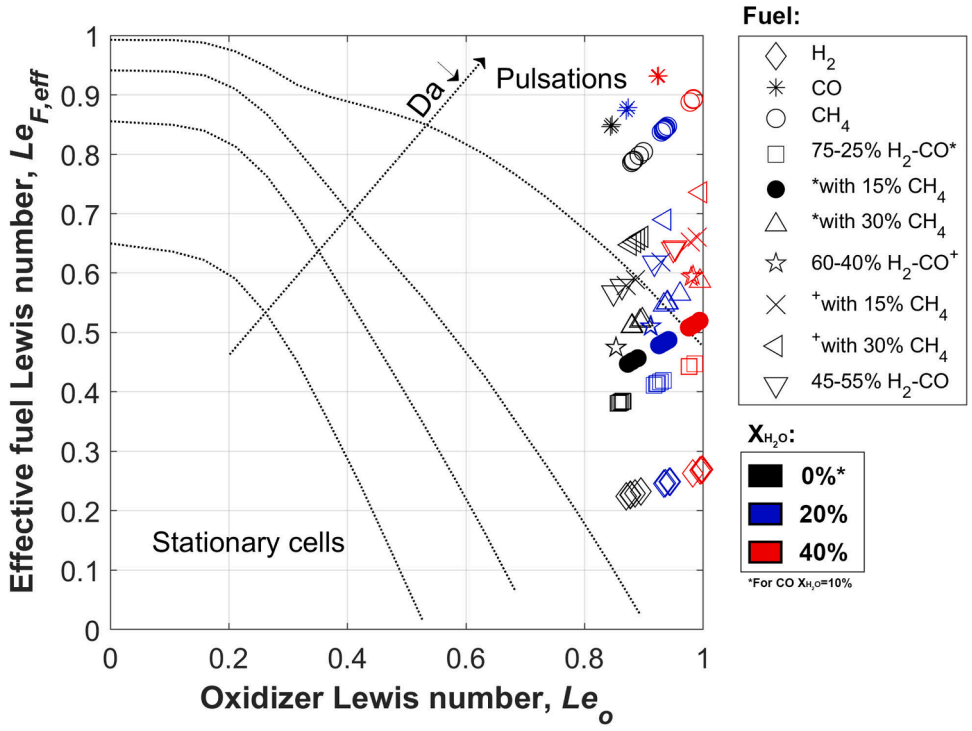

Fig. 10. Effective fuel and oxidizer Lewis numbers for the unstable flames generated in our burner (markers). The instability zones are extracted from the theoretical findings of Cheatham and Matalon at $\phi = 1/3$ [36]. The effect of decreasing the Damköhler number is qualitatively shown by the dotted lines.

dilution, which renders the pulsations faster as explained in subSection 3.2.

When it comes to blends of H_2, CO and CH_4 fuel species, superimposed instability patterns can form [22], whereby CO/CH_4 intensity pulsations onset simultaneously with the cells from H_2. Next, we discuss the effect of H_2O dilution on these instabilities which can be

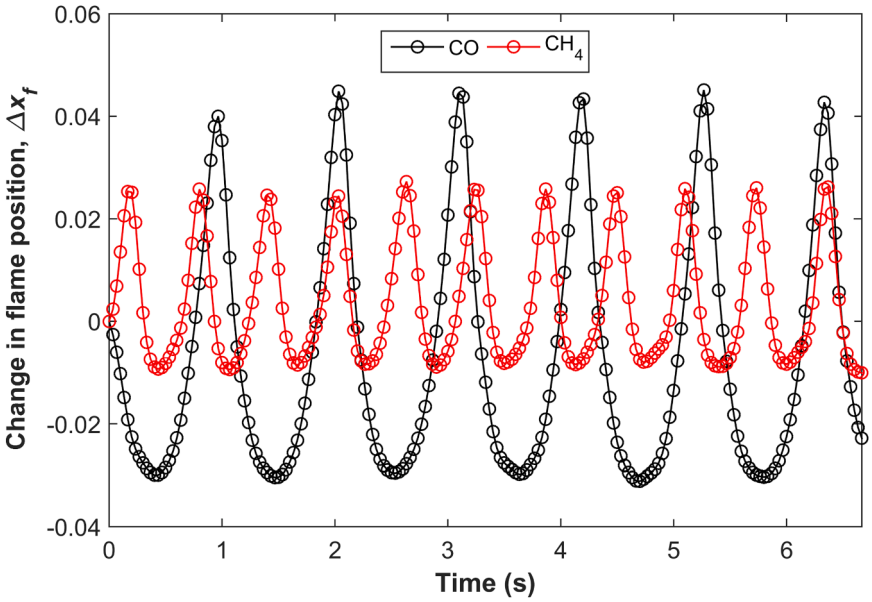

Fig. 11. Illustration of the typical planar intensity pulsations for CO (0.92 Hz) and CH_4 (1.62 Hz).

categorized as: 1) pulsation-induced, or 2) inherently cellular.

3.1.1. *Pulsation-induced instabilities*

Fig. 12 shows the instability patterns that occur in 75–25% H_2-CO flames at different X_{H_2O}. The effect of adding CH_4 or varying the CO content is discussed later. It can be seen that pulsation-induced superimposed instabilities occur at relatively large Damköhler numbers. As the 75–25% H_2-CO flame transitions into instability beyond the marginal stability state $D_a = 1$ at $X_{H_2O} =$ 0%, spatially-homogenous perturbations in its chemical reaction rate develop at a CO-attributed frequency of 0.8 Hz across the planar flame front. Within a few seconds, the intensity of these CO-driven planar pulsations dramatically grows, and the combustion intensity at the lowest point of the instability cycle becomes sufficiently low to momentarily provide the low Damköhler number conditions where completely detached H_2-attributed cells form, as shown in Fig. 13a) (pos. 2). As the burning intensity increases along the pulsation wave, the amplitude of the cells grows in-phase (pos. 3), and they eventually merge together as the highest intensity point of pulsation is approached, after which the flame is temporarily no longer cellular (pos. 4), before the repetition of the cycle. Therefore, given that the pulsations control the instability frequency and the appearance of cells, these superimposed effects were labelled pulsation-induced cellular flames, as shown in supplemental video 1.

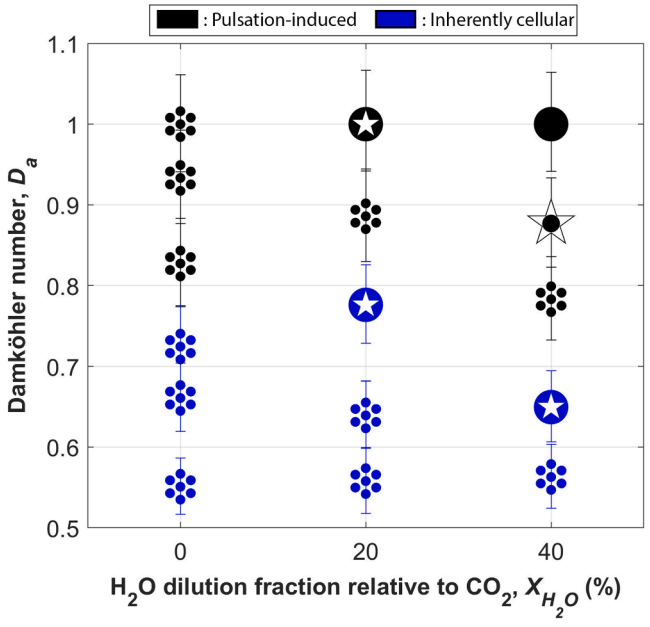

Fig. 12. Variation in the instability patterns with H_2O fraction relative to CO_2 at different Damköhler numbers for 75–25% H_2-CO. The symbols indicate the shape of the instability: (●): planar intensity pulsations, (✷): travelling waves, (✪): partly cellular, and (□): fully cellular. The mean initial mixture strength is 0.55 with 0.13 standard deviation.

When the water fraction in the diluting stream increases from $X_{H_2O} =$ 0 to 20%, the cells that are induced by the pulsations at $D_a = 1$ are no longer completely detached from each other. Such a partly cellular pulsation-induced flame is shown in Fig. 13b). Upon further increasing the water fraction to $X_{H_2O} =$ 40%, no cellular instabilities of any degree are observed in the vicinity of the marginal stability state, as the pulsations become essentially planar as shown in Fig. 13c) and supplemental video 2. The addition of H_2O as a diluent, replacing part of the CO_2, has therefore suppressed the cellular character of the superimposed instability mode observed at marginal stability for 75–25% H_2-CO.

A similar reduction in the propensity of cellular instabilities forming as H_2O replaces CO_2 can also be noticed at other Damköhler numbers in Fig. 12. For instance, at $D_a \approx 0.9$, the pulsations result in travelling waves when X_{H_2O} is set to 40%, instead of forming fully cellular flames when $X_{H_2O} \leq 20\%$. The reduction in the degree of pulsation-induced cellularity at higher water fractions is attributed to the increase in the fuel and oxidizer Lewis numbers. As X_{H_2O} increases from 0 to 40% in 75–25% H_2-CO, $Le_{F,eff}$ increases from 0.38 to 0.44, and Le_o from 0.86 to 0.98, as reported in Fig. 10.

Fig. 12 also shows that cellularity increases as the Damköhler number decreases when moving further from the marginal stability state, which is consistent with the behaviour of H_2 flames that was discussed earlier. For instance, at $X_{H_2O} = 40\%$, the instabilities in 75–25% H_2-CO flames transition from planar intensity pulsations at the marginal stability state, to pulsations-induced travelling waves at $D_a \approx 0.9$, to pulsations-induced fully cellular flames at $D_a \approx 0.8$. Eventually however, as the combustion intensity is rendered sufficiently weak, the flame transitions into the second category of superimposed instabilities: inherently cellular.

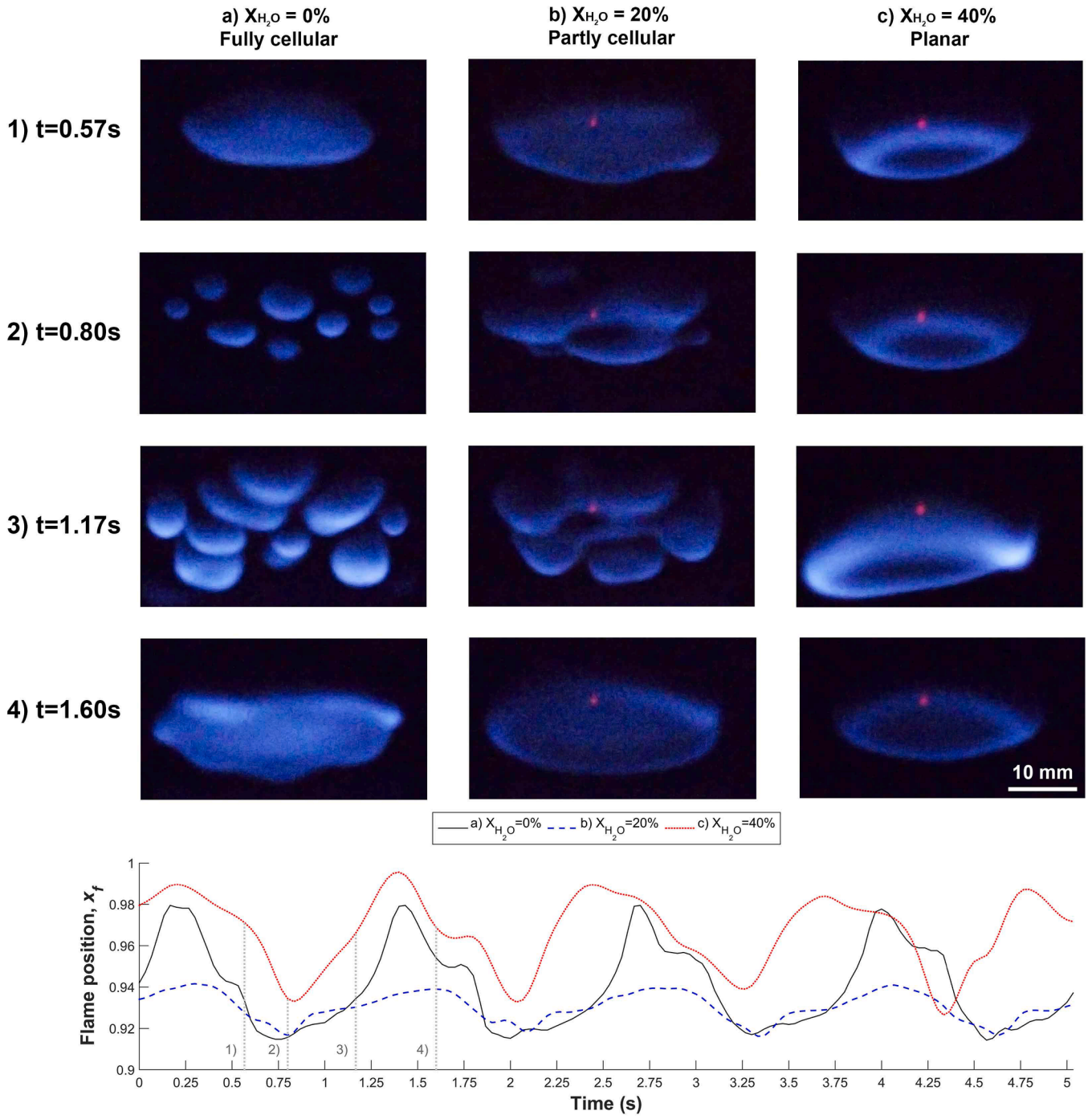

Fig. 13. Effect of the H_2O dilution fraction on the pulsation-induced instabilities at 75–25% H_2-CO, $D_a = 1.0$ and $\phi \approx 0.55$ (supplemental video 2).

3.1.2. *Inherently cellular instabilities*

At sufficiently small Damköhler numbers, intensity pulsations are no longer required to turn the H_2-rich fuel mixture cellular. Fully cellular stationary flames with no intensity pulsations similar to those of Fig. 9c) are observed at $D_a \approx 0.73$ for 75–25% H_2-CO with $X_{H_2O} = 0\%$. However, as the CO chemical reaction rate perturbations grow when D_a is reduced in the now inherently cellular multi-fuel flame, they become superimposed locally within each detached cell, instead of uniformly across a connected flame sheet, resulting in pulsations that are out-of-phase across a fragmented flame. Relative to the previously discussed pulsation-induced cellular flame that forms at larger Damköhler numbers, the oscillations are now minimally dampened, with relatively fast frequencies that exceed 3 Hz, and with intensities that always grow unsustainably with time, leading to temporary extinction areas within the flame as shown in Fig. 14. The extinct cells are then replenished with ones undergoing earlier stages of the same pulsation cycle. Such inherently cellular pulsating flames occur near the lean extinction limit, and are compared to pulsation-induced cells in supplemental video 3.

Increasing the fraction of H_2O dilution decreases the Damköhler number range where such inherently cellular instabilities form, as can be seen from Fig. 12. Lower Damköhler numbers are as a result required to transition from the pulsation-induced mode to the inherently cellular one. For instance, at $X_{H_2O} = 20\%$, inherently fully cellular flames first form at $D_a \approx 0.63$, instead of $D_a \approx 0.73$ when no water is added. At $X_{H_2O} = 40\%$, their onset is further pushed towards the lean extinction limit, $D_a \approx 0.56$. Fig. 15 shows the typical chemiluminescence of a single

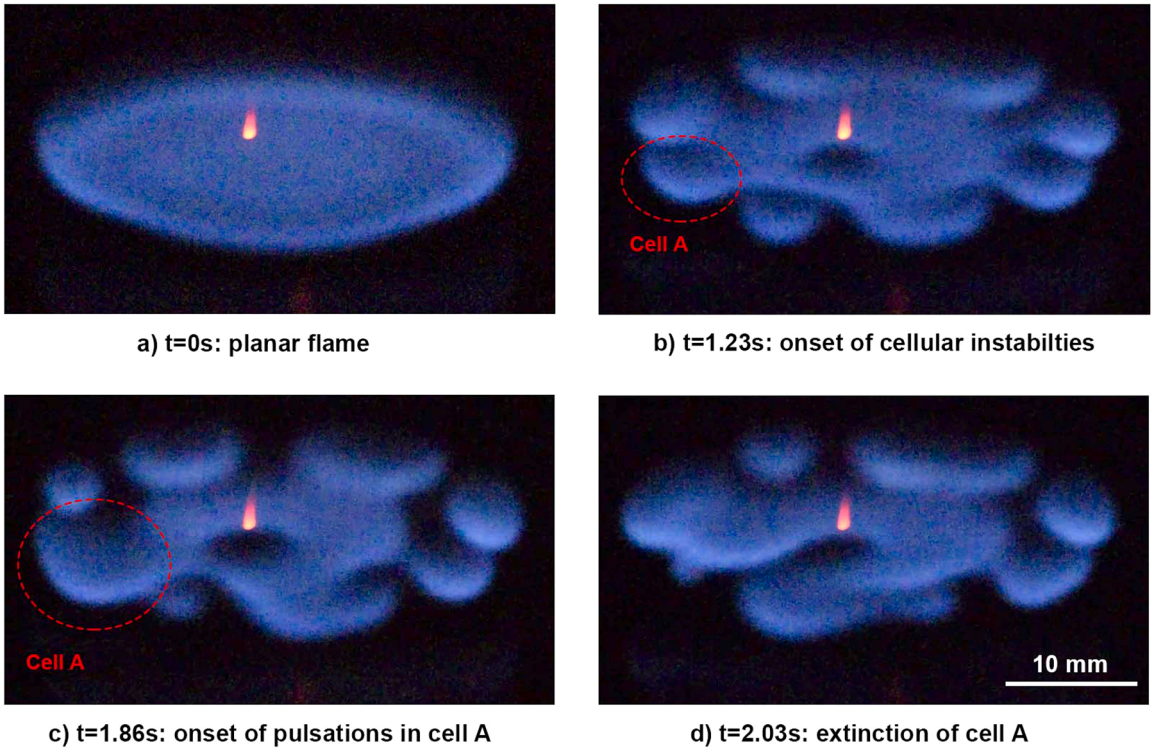

Fig. 14. Development of inherently cellular pulsating instabilities at 75–25% H_2-CO, $D_a = 0.56$ and $\phi = 0.38$.

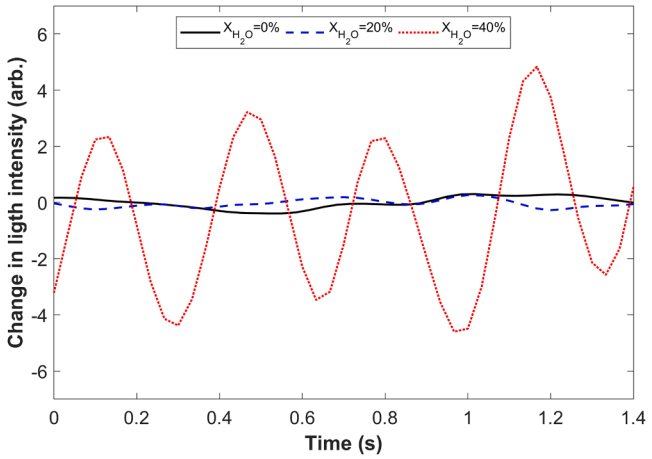

Fig. 15. Typical variation in the light intensity of a single cell in 75–25% H_2-CO with a) $X_{H_2O} = 0\%$ ($D_a = 0.73$), b) $X_{H_2O} = 20\%$ ($D_a = 0.63$), and c) $X_{H_2O} = 40\%$ ($D_a = 0.56$), at the transitioning point into inherent cellular instabilities.

cell at the transitioning point into the inherently cellular instability regime. It can be seen that at $X_{H_2O} =$ 40%, the inherently cellular flames are never stationary and always exhibit pulsations, unlike at $X_{H_2O} \leq$ 20% ($Le_{F,eff} \leq 0.4$) where the light signals are relatively stable. Stationary cells are also never observed at $X_{H_2O} = 0\%$ when 15% CH_4 is added to 75–25 H_2-CO, or when CO is increased to 60–40% H_2-CO. Pulsations always accompany cellular instabilities for these blends. Although their composition is different, these mixtures have $Le_{F,eff} \geq 0.45$ (Fig. 10), the significance of which is highlighted next.

3.1.3. Fuel effective Lewis number

Fig. 16a) shows the instabilities in 75–25% H_2-CO mixtures to which 15% CH_4 is added. Even at $X_{H_2O} = 0\%$, planar intensity pulsations form near marginal stability, before the formation of pulsation-induced cells, followed by inherently cellular flames at smaller Damköhler numbers. Such patterns are similar to the CH_4-free case with $X_{H_2O} = 40\%$ (Fig. 12), which happens to attain a similar $Le_{F,eff} \approx 0.45$.

In Fig. 16b), the quantity of CH_4 relative to the other fuel species is increased to 30%. Superimposed instabilities are observed at $X_{H_2O} = 0\%$, and to a lower extent at $X_{H_2O} =$ 20%, where $Le_{F,eff} \approx 0.51$ and 0.55, respectively. As X_{H_2O} is increased to 40% and $Le_{F,eff}$ becomes approximately equal to 0.6, only planar intensity pulsations form. Similarly, planar instabilities are also observed for CH_4-free mixtures whose CO content is increased to 60–40% H_2-CO (Fig. 16c) at $X_{H_2O} = 40\%$, where the Lewis number is also $Le_{F,eff} \approx 0.6$. In fact, upon comparing Fig. 16b) and c), one can immediately notice the resemblance in the instability patterns for a given water fraction. As shown in Fig. 10, the two different fuel blends attain the same $Le_{F,eff}$ and Le_o.

As the CO content is increased to 45–55% H_2-CO, or as 30% CH_4 is added to the 60–40% H_2-CO mixture, planar intensity pulsations become the only instability observed for all unstable Damköhler numbers, even at $X_{H_2O} = 0\%$. For these blends, $Le_{F,eff} \geq 0.59$. Water dilution nonetheless affects the pulsation frequency of these non-cellular flames, as discussed in the next section.

The aforementioned instability patterns were also reported at the same $Le_{F,eff}$ intervals in our previous experiments with the mark II version of the burner [22]. However, varying the relative amount of combustible species was the only way to control $Le_{F,eff}$, as only CO_2 was used as a diluent. The incorporation of a second diluting species in the current study offers additional means to control $Le_{F,eff}$, and consequently, more evidence on its fundamental significance.

It should be noted that unlike for single-reactant fuels, multiple *Le* formulations have been proposed in the literature to consider the diffusivity of each reactant in multi-fuel mixtures. Amongst these formulations is a molar-based *Le*, which is adopted in the current study, and a heat release-based approach, which weighs the Lewis number of each species by its non-dimensional heating value. These were recently compared by Lapalme et al. [37], where it was shown that for laminar H_2/CO/CH_4 flames, an effective *Le* based on the mole fractions of each

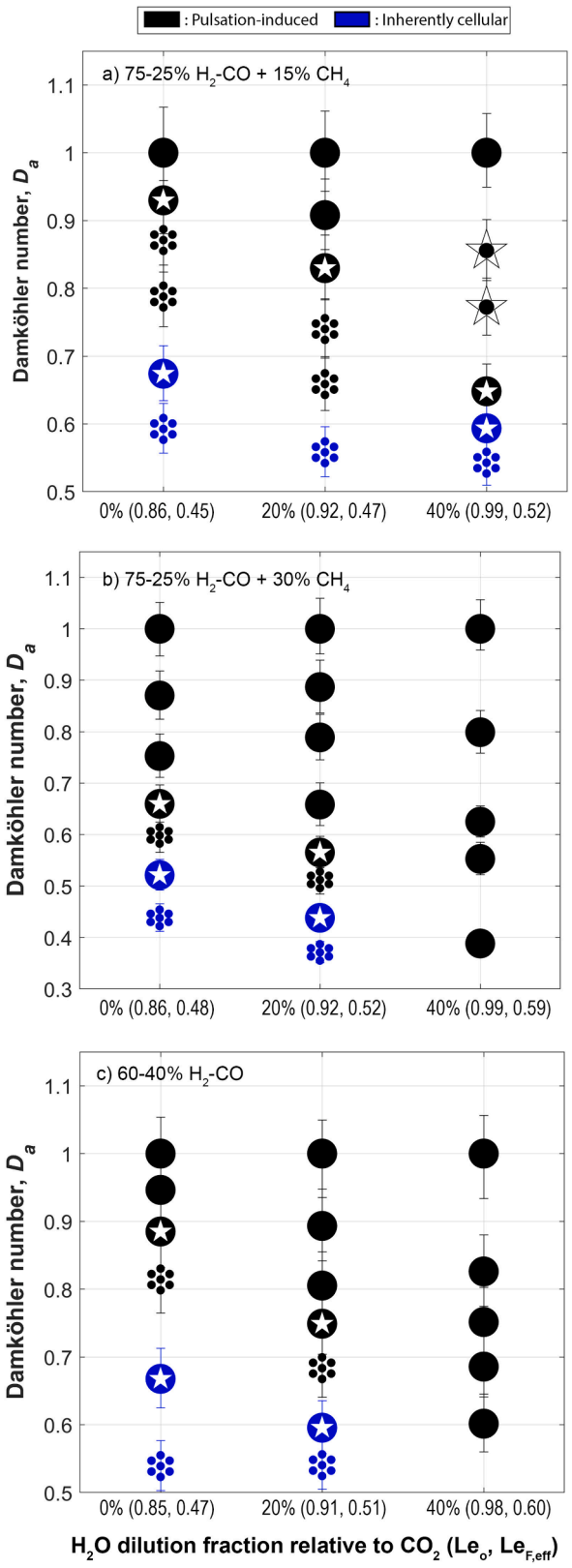

Fig. 16. Variation of the instability patterns with H_2O fraction relative to CO_2 for a) 60–40% H_2-CO, b) 75–25% H_2-CO + 15% CH_4, and c) 75–25% H_2-CO + 30% CH_4. The symbols indicate the type of instability: (●): planar intensity pulsations, (✱): travelling waves, (✪): partly cellular, and (□): fully cellular. The mean initial mixture strength is 0.61 with 0.17 standard deviation.

species is the closest match to experimentally-extracted *Le* (evaluated using integral and asymptotic analyses). We compared these two definitions and also conclude that the heat release-based *Le* does not capture the trends observed in our experiments data. For instance, such fuel *Le* formulation does not increase with the addition of 30% CH_4 to syngas, failing to capture the reduction in the propensity for cellular instabilities that is observed experimentally. It is worth noting however, that this discussion pertains to laminar flames, and other *Le* formulations could become relevant in turbulent systems.

Consequently, Fig. 17 shows a generalized instability map in terms of $Le_{F,eff}$ that is applicable to unstrained diffusion flames of any mixture of H_2-CO-CH_4 fuel species diluted in H_2O and CO_2 with the initial mixture strength being approximately $\phi \approx 0.6$ and the oxidizer Lewis number $Le_o \approx 0.95$. The effect of increasing the latter two parameters on the instability patterns is qualitatively shown by the dashed horizontal axis.

3.2. Effect of H_2O dilution on the instability size

3.2.1. Number of cells

Fig. 18a) presents a box plot of the number of cells (N_{cells}) observed in pulsation-induced cellular flames at different water vapor concentrations relative to CO_2. The cells are measured at the lowest intensity point of the pulsation cycle, for all the unstable flames that are observed from marginal stability to the lean extinction limit. The data show that the number of cells induced by pulsations decreases as H_2O replaces CO_2. For the 75–25% H_2-CO mixture, the median number of cells is 9, which decreases to 6 at $X_{H_2O} = 20\%$, and down to 4 cells at $X_{H_2O} = 40\%$. A similar trend is observed with the other H_2-CO-CH_4 blends, where it can also be noted that N_{cells} also decreases as the H_2 content is reduced. Similarly, the reduction in N_{cells} with water fraction in inherently cellular pulsating flames is also presented in Fig. 18b). Compared to pulsation-induced ones, N_{cells} of inherently cellular flames is generally larger.

In our circular cross-section combustion chamber, the cell spacing (λ_c) is the arc length of a circle that passes through the centroid of each of the outermost cell. Given that it is inversely proportional to the number of cells, λ_c exhibits the opposite behaviour with X_{H_2O}, as also shown in Fig. 18. Furthermore, in unstrained diffusion flames, the cell size is expected to scale as [36]:

$$\lambda_c \sim 2\pi l_D/\sigma^* \tag{6}$$

with $l_D = D_{th}/U$ being the diffusion length, and σ^* the instability wavenumber, or the dimensionless instability wavelength, which is a fundamental parameter that has been shown to decrease with Le_F in theoretical work [17]. This is confirmed experimentally after computing the instability wavenumbers of our inherently cellular flames, as shown in Fig. 19. The tendency of σ^* to drop with $Le_{F,eff}$ is evident, for all the initial mixture strengths considered. Given that $Le_{F,eff}$ increases with X_{H_2O}, this provides an explanation for the increased cell spacing or reduced number of cells at higher X_{H_2O}.

3.2.2. Pulsation frequency

Fig. 20 shows the effect of the water dilution fraction on the frequency (f) of pulsation-induced unstable flames. Both cellular and planar pulsating flames are considered. Unlike the number of cells, the data show that the pulsation frequency increases as H_2O replaces CO_2. For instance, at 75–25% H_2-CO with 15% CH_4, the median frequency increases from 0.91 Hz at $X_{H_2O} = 0\%$, to 1.04 Hz at $X_{H_2O} = 20\%$, and eventually to 1.32 Hz at $X_{H_2O} = 40\%$. This trend is observed for all H_2-CO-CH_4 fuel blends, across which the frequency is highest for a given X_{H_2O} at the highest CH_4 content. This is consistent with our earlier discussion with single-fuel flames, where CH_4 is shown to pulsate faster than CO.

The non-dimensional frequency is expressed as:

$$\widetilde{f} = 2\pi f D_{th}/U^2 \tag{7}$$

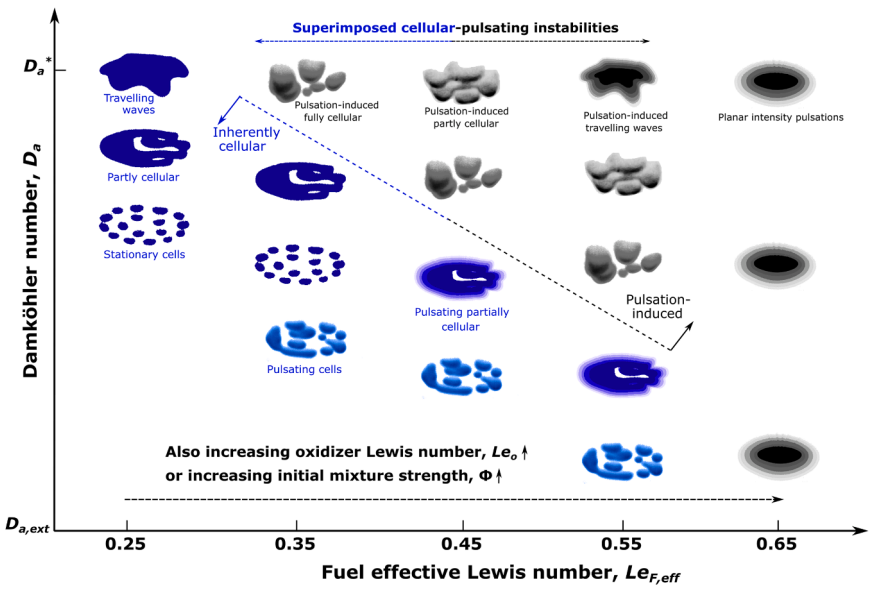

Fig. 17. Illustration of the sustained instability patterns observed as a function of the effective fuel Lewis number for H_2-CO-CH_4 mixtures diluted in H_2O and CO_2 at $\phi \approx 0.6$ and $Le_o \approx 0.95$. The effect of increasing Le_o or ϕ is qualitatively shown by the dashed horizontal axis.

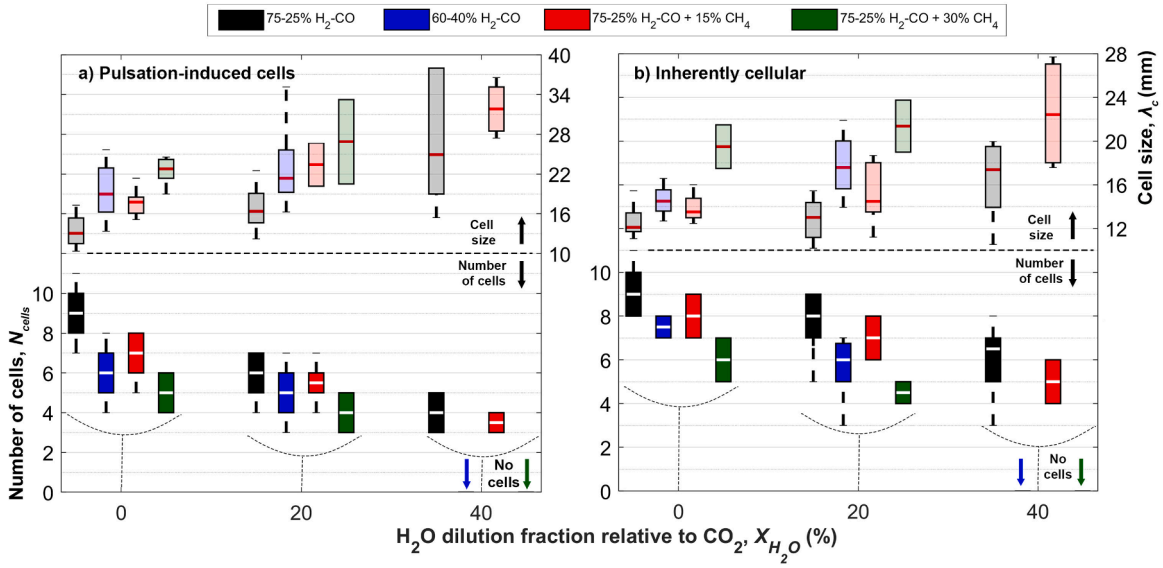

Fig. 18. Variation in the number and size of cells as a function of the water fraction for a) pulsation-induced cells and b) inherently cellular flames. Box: 25th and 75th percentile, line within the box: median value, and whiskers: minimum and maximum values. The mean initial mixture strength is 0.59 with 0.18 standard deviation.

and theoretical results [17] show that $\widetilde{f}$ increases with Le_F, and therefore X_{H_2O}, as we confirm in Fig. 21, where a broad range of initial mixture strengths is considered. It can be seen that at a given ϕ, the larger the $Le_{F,eff}$, the higher the non-dimensional pulsation frequency. Consistent with theoretical predictions, it can also be seen that the pulsation frequency increases with initial mixture strength. In fact, the trend appears to be highly linear over a given $Le_{F,eff}$ interval for the conditions tested, as seen from the three fitted lines.

4. Conclusion

This paper introduces a new version of the unstrained diffusion flame burner which is used to study the effect of H_2O dilution on diffusive-thermal instabilities in H_2-CO-CH_4 fuels. Obtaining fundamental insight on such complex phenomena is considerably facilitated by the absence of significant hydrodynamic or buoyancy-driven disturbances, which are parasitic effects omnipresent in common research facilities. The counter-diffusion burner used adopts an evenly heated aluminum perforated injector, to uniformly supply the H_2O-containing fuel mixture into the bottom of the combustion chamber. The nominally one-dimensional nature of the flow in the reaction zone is confirmed by measuring the major species concentration profiles and flame location, which are in excellent agreement with the one-dimensional chambered diffusion flame solution.

Experimentally measured flame stability and extinction limits are provided for a broad range of fuel blends diluted at different H_2O and CO_2 proportions. Burning wet syngas while its still hot has the advantage of enhancing the thermal efficiency of biomass systems as heat losses are reduced. However, results show that as H_2O replaces CO_2 dilution, the

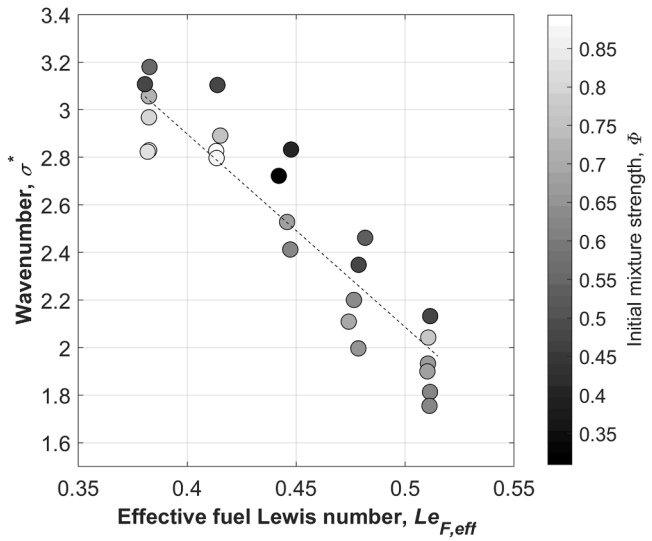

Fig. 19. Instability wavenumber of inherently cellular flames as a function of the effective fuel Lewis number. The color map shows the initial mixture strengths of the flames.

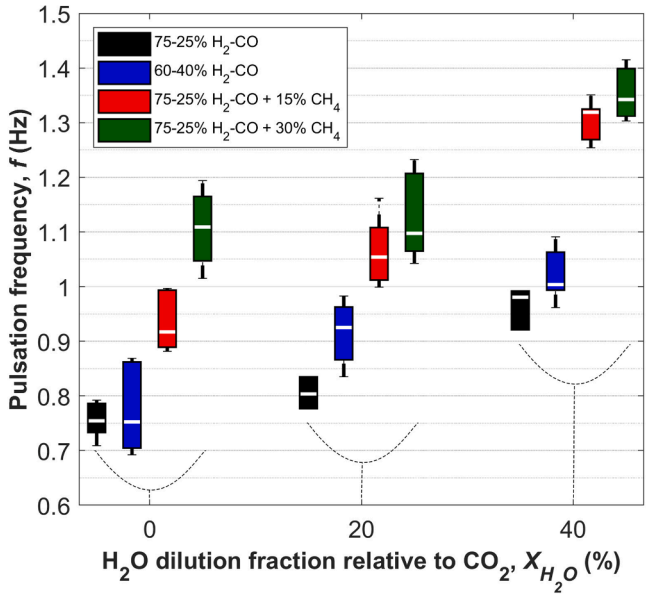

Fig. 20. Frequency as a function of water fraction in the diluting stream for different pulsation-induced unstable flames. Box: 25th and 75th percentile, line within the box: median value, and whiskers: minimum and maximum values. The mean initial mixture strength is 0.59 with 0.18 standard deviation.

low caloric value flame becomes more prone to instabilities and extinction, which must be taken into account in the combustor design. Dilution effect analysis using a one-dimensional diffusion flame model reveals that although the H_2O-diluted mixtures exhibit higher flame temperatures relative to their CO_2-diluted counterparts, due to thermal and chemical effects, the latter is responsible for the reduction in flammability limits as chain terminating and CO_2-H_2O forming reactions are favored.

Beyond marginal stability, the cellular instabilities that onset due to the presence of H_2 are seen to interact and compete with the pulsations from CO and CH_4, leading to cellular-pulsating flames. These superimposed diffusive-thermal instabilities can be categorized as: 1) pulsations-induced, or 2) inherently cellular. The former onset at relatively large Damköhler numbers, and spatially homogenous pulsations

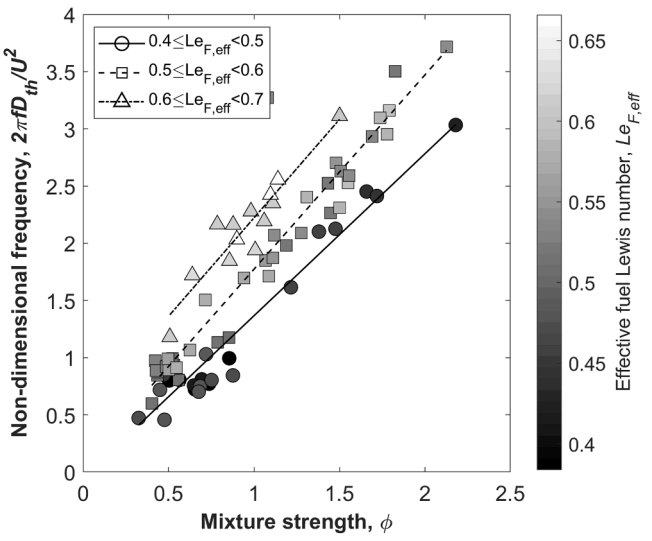

Fig. 21. Non-dimensional pulsation frequency as a function of the initial mixture strength at different effective fuel Lewis numbers.

dictate the instability frequency and the in-phase appearance of cells. At sufficiently small Damköhler numbers, the H_2-containing flame becomes inherently cellular, and as the pulsations now develop, they rapidly grow out-of-phase in each cell, leading to temporary extinction spots in the disconnected flame sheet. In addition, inherently cellular pulsating flames are minimally damped, and are attribute with a relatively fast frequency which exceeds 3 Hz, compared to the 1-Hz frequency of pulsation-induced instabilities.

Increasing the fraction of H_2O dilution relative to CO_2 is shown to reduce the degree of superimposed cellularity, as the oxidizer and fuel Lewis number increase, rendering the pulsating instabilities planar at sufficiently high water content. In addition to the oxidizer Lewis number, the instability types and patterns formed at various fuel compositions are highly dependent on a molar-based fuel effective Lewis number, which weighs the three fuel species Lewis numbers by their relative molar fractions in the fuel stream. The fundamental significance of this parameter is confirmed after obtaining the same instability patterns with different fuels whose $Le_{F,eff}$ is rendered equivalent by changing the proportion of H_2O dilution. Consequently, we demonstrate that in syngas mixtures with $0.85 \leq Le_o \leq 1.0$, superimposed cellular-pulsating instabilities form in the vicinity of $0.37 \leq Le_{F,eff} \leq 0.59$. Above this range, planar intensity pulsations devoid of cellular structures onset, and vice versa at low Lewis numbers. The number of cells that form in the unstable flames decreases with water content, and this is attributed to the fundamental instability wavenumber decreasing at higher $Le_{F,eff}$. On the contrary, larger H_2O dilution fractions increase the frequency of pulsations, as the fundamental non-dimensional frequency increases with $Le_{F,eff}$.

The successful realization of a vaporized fuel unstrained diffusion flame burner that is introduced for the first time in this paper paves the way for various interesting research opportunities. Plans are underway to investigate the unstable flame dynamics of liquid biofuels such as methanol and ethanol in this research facility. Another interesting option would be to study the effect of H_2O dilution on the morphology of soot formation in a one-dimensional flow field which facilitates the comparison with soot models.

5. Novelty and significance statement

An unstrained diffusion flame burner that can be operated with fuels containing high vapor content is introduced for the first time in this paper. Contrary to common research burners, where hydrodynamic

effects play a significant role, nominally unstrained flames are produced in this burner. This paves the way for various novel research opportunities using vaporized biofuels, yielding fundamental insights that could be quantitatively compared to theoretical predictions based on this simple configuration. The focus of this study is diffusive-thermal instabilities that are prone to occur in H_2O-diluted syngas. H_2O dilution can be significant in biomass-derived syngas that is not cooled prior to combustion, and that is often burned directly to lower losses as waste heat and pollutant formation. However, with scarce data on diffusive-thermal instabilities in multi-fuel mixtures, the effect of H_2O dilution on the peculiar superimposed cellular-pulsating flame dynamics that onset in syngas remains unknown.

6. Author contributions

E.A.: Designed research, performed research, analyzed data, wrote the paper.

E.R.: Designed research, analyzed data, reviewed the paper, acquired funding.

Declaration of competing interest

The authors declare that they have no known competing financial interests or personal relationships that could have appeared to influence the work reported in this paper.

Acknowledgements

The authors are grateful for the funders of this work: The Trottier Energy Institute (Trottier scholarship and project grant), the Natural Sciences and Engineering Research Council of Canada (NSERC) through the postgraduate doctoral scholarship (PGSD3 - 546588 – 2020), and discovery grants (RGPIN-03622–2014 and RGPIN-05071–2022), and the Fonds de Recherche du Québec Nature et technologies (FRQNT) through the Doctoral scholarship (B2X).

Supplementary materials

Supplementary material associated with this article can be found, in the online version, at doi:10.1016/j.combustflame.2024.113313.

References

[1] A. Akhtar, V. Krepl, T. Ivanova, A Combined Overview of Combustion, Pyrolysis, and Gasification of Biomass, Energy and Fuels 32 (2018) 7294–7318, https://doi.org/10.1021/acs.energyfuels.8b01678.

[2] S.K. Sansaniwal, K. Pal, M.A. Rosen, S.K. Tyagi, Recent advances in the development of biomass gasification technology: A comprehensive review, Renew. Sustain. Energy Rev. 72 (2017) 363–384, https://doi.org/10.1016/j.rser.2017.01.038.

[3] V. Mislavskii, N. Pestovskii, S. Tskhai, B. Kichatov, V. Gubernov, V. Bykov, U. Maas, Diffusive-thermal pulsations of burner stabilized methane-air flames, Combust. Flame 234 (2021) 111638, https://doi.org/10.1016/J.COMBUSTFLAME.2021.111638.

[4] D. Lapalme, F. Halter, C. Mounaïm-Rousselle, P. Seers, Characterization of thermodiffusive and hydrodynamic mechanisms on the cellular instability of syngas fuel blended with CH4 or CO2, Combust. Flame 193 (2018) 481–490, https://doi.org/10.1016/J.COMBUSTFLAME.2018.03.028.

[5] E. Antar, E. Robert, Thermodynamic analysis of novel methanol polygeneration systems for greenhouses, Biomass Convers. Biorefinery 13 (2023) 8033–8046, https://doi.org/10.1007/s13399-021-01678-5.

[6] M. Matalon, Intrinsic Flame Instabilities in Premixed and Nonpremixed Combustion, Annu. Rev. Fluid Mech. 39 (2007) 163–191, https://doi.org/10.1146/annurev.fluid.38.050304.092153.

[7] O. Armas, R. García-Contreras, Á. Ramos, Pollutant emissions from engine starting with ethanol and butanol diesel blends, Fuel Process. Technol. 100 (2012) 63–72, https://doi.org/10.1016/J.FUPROC.2012.03.003.

[8] S. Yang, A. Saha, Z. Liu, C.K. Law, Role of Darrieus–Landau instability in propagation of expanding turbulent flames, J. Fluid Mech. 850 (2018) 784–802, https://doi.org/10.1017/JFM.2018.426.

[9] V. Molkov, D. Makarov, A. Grigorash, Cellular structure of explosion flames: Modeling and large-eddy simulation, Combust. Sci. Technol. 176 (2004) 851–865, https://doi.org/10.1080/00102200490428495.

[10] R.W. Francisco, A.A.M. Oliveira, Measurement of the adiabatic flame speed and overall activation energy of a methane enriched H2/CO/CO2/N2 low heating value mixture, Int. J. Hydrogen Energy 45 (2020) 29533–29545, https://doi.org/10.1016/j.ijhydene.2020.07.200.

[11] W. Jin, J. Wang, S. Yu, Y. Nie, Y. Xie, Z. Huang, Cellular instabilities of non-adiabatic laminar flat methane/hydrogen oxy-fuel flames highly diluted with CO2, Fuel 143 (2015) 38–46, https://doi.org/10.1016/j.fuel.2014.11.036.

[12] J. Natarajan, T. Lieuwen, J. Seitzman, Laminar flame speeds of H2/CO mixtures: Effect of CO2 dilution, preheat temperature, and pressure, Combust. Flame 151 (2007) 104–119, https://doi.org/10.1016/j.combustflame.2007.05.003.

[13] H.A. Yepes, A.A. Amell, Laminar burning velocity with oxygen-enriched air of syngas produced from biomass gasification, Int. J. Hydrogen Energy 38 (2013) 7519–7527, https://doi.org/10.1016/J.IJHYDENE.2013.03.148.

[14] O. Askari, Z. Wang, K. Vien, M. Sirio, H. Metghalchi, On the flame stability and laminar burning speeds of syngas/O2/He premixed flame, Fuel 190 (2017) 90–103, https://doi.org/10.1016/j.fuel.2016.11.042.

[15] Z. Wang, Z. Bai, G. Yu, S. Yelishala, H. Metghalchi, The Critical Pressure at the Onset of Flame Instability of Syngas/Air/Diluent Outwardly Expanding Flame at Different Initial Temperatures and Pressures, J. Energy Resour. Technol. (2019) 141, https://doi.org/10.1115/1.4042720.

[16] L.. Kirkby, R.A. Schmitz, An Analytical Study of the Stability of a Laminar Diffusion Flame, Combust. Flame 10 (1966) 205–220.

[17] P. Metzener, M. Matalon, Diffusive-thermal instabilities of diffusion flames: onset of cells and oscillations, Combust. Theory Model. 10 (2006) 701–725, https://doi.org/10.1080/13647830600719894.

[18] M. Matalon, P. Metzener, The effect of thermal expansion on diffusion flame instabilities, J. Fluid Mech. 647 (2010) 453–472, https://doi.org/10.1017/S0022112009993016.

[19] D. Lo Jacono, P. Papas, M. Matalon, P.A. Monkewitz, An experimental realization of an unstrained, planar diffusion flame, Proc. Combust. Inst. 30 (2005) 501–509, https://doi.org/10.1016/J.PROCI.2004.07.011.

[20] E. Robert, P.A. Monkewitz, Experiments in a novel quasi-ID diffusion flame with variable bulk flow, Proc. Combust. Inst. 32 I (2009) 987–994, https://doi.org/10.1016/j.proci.2008.06.145.

[21] E. Robert, P.A. Monkewitz, Thermal-diffusive instabilities in unstretched, planar diffusion flames, Combust. Flame 159 (2012) 1228–1238, https://doi.org/10.1016/J.COMBUSTFLAME.2011.10.020.

[22] E. Antar, J. Delavande, E. Robert, Experimental characterization of diffusive-thermal instabilities in CO2-diluted H2CH4CO unstrained diffusion flames, Combust. Flame 250 (2023) 112636, https://doi.org/10.1016/J.COMBUSTFLAME.2023.112636.

[23] H.Y. Shih, J.R. Hsu, Y.H. Lin, Computed flammability limits of opposed-jet H2/CO syngas diffusion flames, Int. J. Hydrogen Energy 39 (2014) 3459–3468, https://doi.org/10.1016/J.IJHYDENE.2013.12.056.

[24] M. Gassner, F. Maréchal, Thermo-economic optimisation of the polygeneration of synthetic natural gas (SNG), power and heat from lignocellulosic biomass by gasification and methanation, Energy Environ. Sci. 5 (2012) 5768–5789, https://doi.org/10.1039/C1EE02867G.

[25] D. Pugh, P. Bowen, A. Valera-Medina, A. Giles, J. Runyon, R. Marsh, Influence of steam addition and elevated ambient conditions on NOx reduction in a staged premixed swirling NH3/H2 flame, Proc. Combust. Inst. 37 (2019) 5401–5409, https://doi.org/10.1016/J.PROCI.2018.07.091.

[26] Y. Wang, M. Gu, Y. Zhu, L. Cao, B. Zhu, J. Wu, Y. Lin, X. Huang, A review of the effects of hydrogen, carbon dioxide, and water vapor addition on soot formation in hydrocarbon flames, Int. J. Hydrogen Energy 46 (2021) 31400–31427, https://doi.org/10.1016/J.IJHYDENE.2021.07.011.

[27] F. Liu, J.L. Consalvi, A. Fuentes, Effects of water vapor addition to the air stream on soot formation and flame properties in a laminar coflow ethylene/air diffusion flame, Combust. Flame 161 (2014) 1724–1734, https://doi.org/10.1016/J.COMBUSTFLAME.2013.12.017.

[28] E. Robert, P.A. Monkewitz, Experimental realization and characterization of unstretched planar one-dimensional diffusion flames, Combust. Flame 160 (2013) 546–556, https://doi.org/10.1016/J.COMBUSTFLAME.2012.11.011.

[29] É. Robert, Experimental Investigation of Unstrained Diffusion Flames and their Instabilities, PhD thesis, Ecole Polytechnique Federale de Lausanne, 2008.

[30] E. Robert, Mass spectrometer calibration over wide concentration ranges in multicomponent gas mixtures, Meas. Sci. Technol. (2010) 21, https://doi.org/10.1088/0957-0233/21/2/025102.

[31] D.G. Goodwin, R.L. Speth, H.K. Moffat, B.W. Weber, Cantera: An Object-oriented Software Toolkit for Chemical Kinetics, Thermodynamics, and Transport Processes, (2021). doi:10.5281/zenodo.4527812.

[32] S. Chandrasekhar, Hydrodynamic and hydromagnetic stability, 1961.

[33] N. Peters, Laminar diffusion flamelet models in non-premixed turbulent combustion, Prog. Energy Combust. Sci. 10 (1984) 319–339, https://doi.org/10.1016/0360-1285(84)90114-X.

[34] H.Y. Shih, J.R. Hsu, Dilution effects analysis of opposed-jet H2/CO syngas diffusion flames, Combust. Theory Model. 17 (2013) 543–562, https://doi.org/10.1080/13647830.2013.782069.

[35] P. Metzener, M. Matalon, Onset of cells and oscillations in diffusion flames, 44th AIAA Aerosp. Sci. Meet. Exhib. (2006) 1167, https://doi.org/10.2514/6.2006-1167.

[36] S. Cheatham, M. Matalon, A general asymptotic theory of diffusion flames with application to cellular instability, J. Fluid Mech. 414 (2000) 105–144, https://doi.org/10.1017/S0022112000008752.

[37] D. Lapalme, R. Lemaire, P. Seers, Assessment of the method for calculating the Lewis number of H2/CO/CH4 mixtures and comparison with experimental results,

Int. J. Hydrogen Energy 42 (2017) 8314–8328, https://doi.org/10.1016/J.IJHYDENE.2017.01.099.